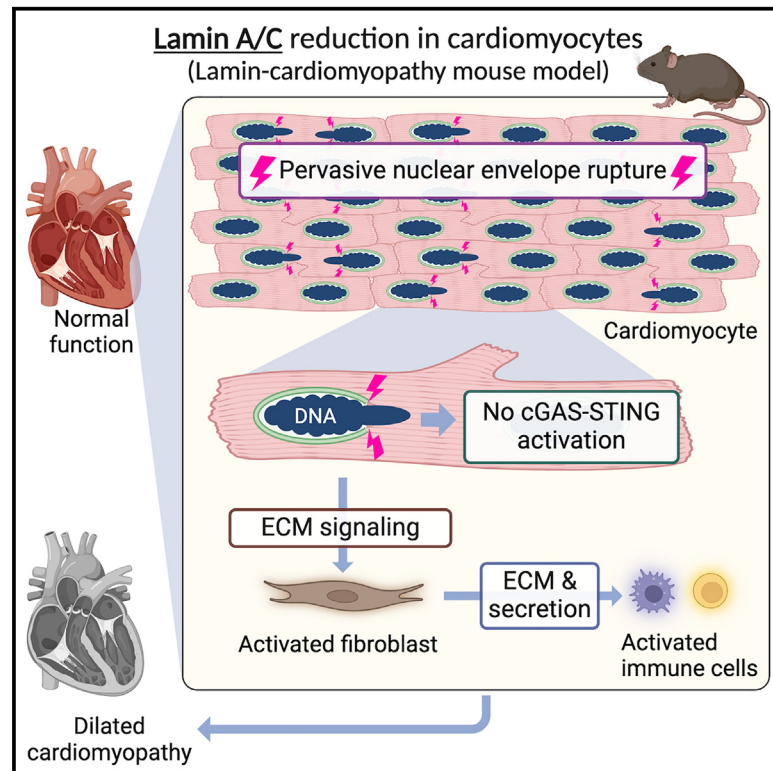# Pervasive nuclear envelope ruptures precede ECM signaling and disease onset without activating cGAS-STING in Lamin-cardiomyopathy mice

Graphical abstract

Authors

Atsuki En, Hanumakumar Bogireddi, Briana Thomas, ..., Peter Pytel, Ivan P. Moskowitz, Kohta Ikegami

Correspondence

kohta.ikegami@cchmc.org

In brief

En et al. report pervasive nuclear envelope ruptures in cardiac myocytes in a mouse model of nuclear lamin-related cardiomyopathy. Surprisingly, nuclear envelope ruptures do not activate cGAS-STING cytosolic DNA-sensing innate immunity in hearts. Instead, ECM signaling from Lamin-mutant cardiomyocytes is predicted to initiate an inflammatory response.

Highlights

- Lamin A/C reduction causes pervasive nuclear envelope ruptures in cardiomyocytes

- Nuclear envelope ruptures do not activate cGAS-STING pathway in cardiomyocytes

- cGAS-STING does not contribute to Lamin A/C-dependent cardiomyopathy in adult mice

- ECM signaling from Lamin-reduced cardiomyocytes may initiate inflammatory response

CellPress

Report

Pervasive nuclear envelope ruptures precede ECM signaling and disease onset without activating cGAS-STING in Lamin-cardiomyopathy mice

Atsuki En,[1,2] Hanumakumar Bogireddi,[1] Briana Thomas,[1,7] Alexis V. Stutzman,[3,8] Sachie Ikegami,[3,9] Brigitte LaForest,[3,10] Omar Almakki,[3,11] Peter Pytel,[4] Ivan P. Moskowitz,[3,4,5] and Kohta Ikegami[1,6,12,*]

[1]Division of Molecular Cardiovascular Biology, Cincinnati Children's Hospital Medical Center, Cincinnati, OH 45229, USA
[2]Graduate School of Nanobioscience, Yokohama City University, Yokohama, Kanagawa 236-0027, Japan
[3]Department of Pediatrics, the University of Chicago, Chicago, IL 60637, USA
[4]Department of Pathology, the University of Chicago, Chicago, IL 60637, USA
[5]Department of Human Genetics, the University of Chicago, Chicago, IL 60637, USA
[6]Department of Pediatrics, University of Cincinnati College of Medicine, Cincinnati, OH 45267, USA
[7]Present address: Medpace, Cincinnati, OH 45227, USA
[8]Present address: Curriculum in Genetics & Molecular Biology, the University of North Carolina at Chapel Hill, Chapel Hill, NC 27599, USA
[9]Present address: Hoxworth Blood Center, University of Cincinnati, Cincinnati, OH 45267, USA
[10]Present address: Pfizer Worldwide Research, Development & Medical, Cambridge, MA 02139, USA
[11]Present address: Indiana University School of Medicine, Indiana, IN 46202, USA
[12]Lead contact
*Correspondence: kohta.ikegami@cchmc.org
https://doi.org/10.1016/j.celrep.2024.114284

SUMMARY

Nuclear envelope (NE) ruptures are emerging observations in Lamin-related dilated cardiomyopathy, an adult-onset disease caused by loss-of-function mutations in Lamin A/C, a nuclear lamina component. Here, we test a prevailing hypothesis that NE ruptures trigger the pathological cGAS-STING cytosolic DNA-sensing pathway using a mouse model of Lamin cardiomyopathy. The reduction of Lamin A/C in cardio-myocyte of adult mice causes pervasive NE ruptures in cardiomyocytes, preceding inflammatory transcription, fibrosis, and fatal dilated cardiomyopathy. NE ruptures are followed by DNA damage accumulation without causing immediate cardiomyocyte death. However, cGAS-STING-dependent inflammatory signaling remains inactive. Deleting cGas or Sting does not rescue cardiomyopathy in the mouse model. The lack of cGAS-STING activation is likely due to the near absence of cGAS expression in adult cardiomyocytes at baseline. Instead, extracellular matrix (ECM) signaling is activated and predicted to initiate pro-inflammatory communication from Lamin-reduced cardiomyocytes to fibroblasts. Our work nominates ECM signaling, not cGAS-STING, as a potential inflammatory contributor in Lamin cardiomyopathy.

INTRODUCTION

Lamin A/C (LMNA) are nuclear lamina proteins that provide structural integrity to the nuclear envelope (NE).[1–4] Mutations in LMNA cause a spectrum of degenerative disorders, collectively called laminopathies, including frequent dilated cardiomyopathy (LMNA-related DCM).[5–10] LMNA-related DCM is a prevalent adult-onset disease[11,12] that accompanies cardiac conduction disease, fibrosis, heart failure, and mortality.[13–16] LMNA-related DCM is predominantly caused by heterozygous loss-of-function LMNA mutations that cause Lamin A/C protein reduction most strongly in cardiomyocytes.[16–20] Activation of stress-response-related signaling, such as mitogen-activated protein kinase signaling,[21–24] mTOR signaling,[25] and DNA damage response signaling,[26,27] has been reported in LMNA-related DCM models. However, the direct pathological alterations caused by Lamin A/C reduction in cardiomyocytes remain undefined.

Reduction of nuclear lamins can cause ruptures of the NE (NE ruptures).[28–34] Indeed, NE ruptures have been observed in patients,[17,18,35–37] animal models,[30,31,38–42] and cell culture models[30,34] of LMNA-related DCM and laminopathies. However, the extent of NE ruptures in LMNA-related DCM and the contribution of this event to the pathogenesis of DCM remain undefined.

A prevailing hypothesis for LMNA-related DCM pathogenesis implicates the cGAS-STING pathway as a link between NE rupture, inflammatory signaling, and DCM pathogenesis.[39,40,43–45] cGAS-STING is a cytosolic DNA-sensing innate immune mechanism, in which cGAS binds to cytosolic DNA and activates cell-autonomous STING-mediated interferon transcription.[46,47] cGAS-STING pathway activation has been observed in a cellular model of progeria[48] and Lmna-knockout developing hearts.[27] cGAS-STING activation has also been reported in mouse models of other heart diseases.[49–52] However,
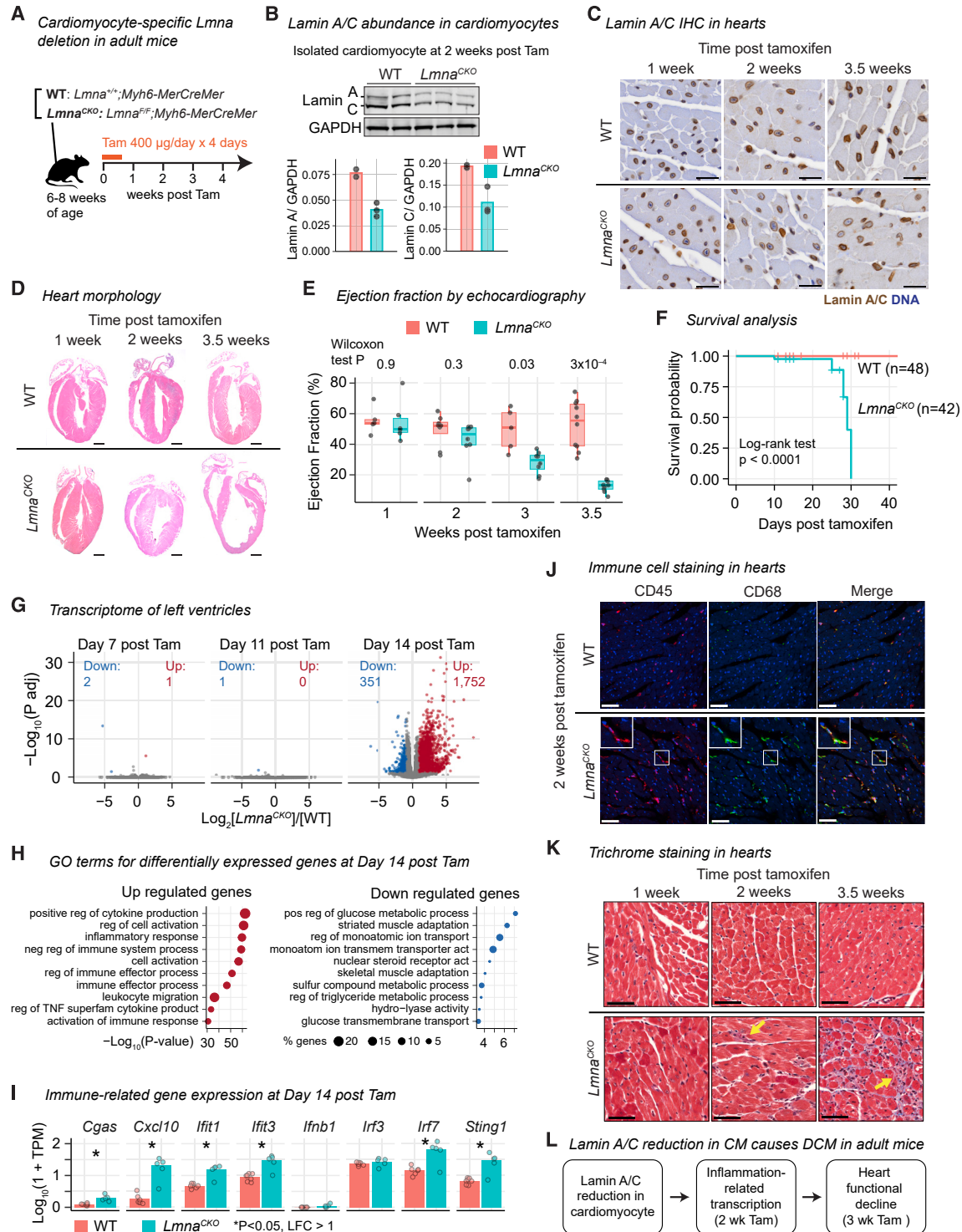
Figure 1. Lamin A/C reduction in cardiomyocytes causes dilated cardiomyopathy in adult mice

(A) Tamoxifen (Tam) induces *Lmna* deletion in cardiomyocytes in adult mice. See Figure S1 for related analyses.

(B) Lamin A/C immunoblot in isolated cardiomyocytes (top) with signal quantification (bottom). *n* = 2–3 mice/genotype.

(C) Lamin A/C immunohistochemistry (brown) with hematoxylin counterstaining (blue) in mouse heart tissues. Scale bar: 20 μm.

(D) Hematoxylin and eosin staining of hearts. Scale bar: 1 mm.

(E) Left ventricular ejection fraction with interquartile range (box) measured by echocardiography. *p* value, Wilcoxon test. *n* = 5–10 mice/genotype.

(F) Kaplan-Meier survival analysis. Wild type (WT) *n* = 48, *Lmna^CKO^* *n* = 42. *p* value, log-rank test.

(legend continued on next page)

a direct link between NE ruptures and the cGAS-STING activation in *LMNA*-related DCM remains undefined. In this study, we report pervasive NE ruptures prior to DCM development and provide evidence against the hypothesis that cGAS-STING activation contributes to *LMNA*-related DCM. Instead, our study nominates a role for extracellular matrix (ECM) signaling from cardiomyocytes in this disease.

RESULTS

Lamin A/C reduction in cardiomyocytes causes DCM in adult mice

We generated a mouse model of *LMNA*-related DCM using cardiomyocyte-specific deletion of *Lmna* (*Lmna^F/F^;Myh6-Mer-CreMer*, called *Lmna^CKO^* hereafter) and littermate control wild-type mice (*Lmna^+/+^;Myh6-MerCreMer*) (Figures S1A and S1B). *Lmna* deletion in cardiomyocytes was induced by tamoxifen administration to adult mice at 6–8 weeks of age (Figure 1A). Lamin A and Lamin C proteins were 47% and 43% reduced, respectively, in cardiomyocytes of *Lmna^CKO^* mice at 2 weeks post-tamoxifen by immunoblots, consistent with the ∼4-week half-life of Lamin A/C in mouse hearts[53] (Figures 1B and S1C). Reduced, but persistent, Lamin A/C in individual cardiomyocytes was confirmed at 1, 2, and 3.5 weeks post-tamoxifen by tissue staining (Figure 1C). Thus, *Lmna^CKO^* mice reproduced the Lamin A/C protein insufficiency, not elimination, observed in cardiomyocytes of patients with *LMNA*-related DCM.[18,20]

*Lmna^CKO^* mice developed progressive DCM as reported previously.[38] Hearts of *Lmna^CKO^* mice were indistinguishable from wild-type hearts in gross morphology (Figure 1D) and contractile activity measured by echocardiography (Figure 1E) until 2 weeks post-tamoxifen. However, at 3 weeks post-tamoxifen, the left ventricular ejection fraction, an indicator of cardiac systolic function, significantly diminished (Figure 1E). At 3.5 weeks post-tamoxifen, *Lmna^CKO^* hearts became severely dilated, with a significant reduction of ventricular wall thickness and loss of systolic activity (Figures 1D, 1E, and S1D). *Lmna^CKO^* mice invariably died between 3.5 and 4.5 weeks post-tamoxifen (Figure 1F). Thus, the modest reduction of Lamin A/C in cardiomyocytes was sufficient to cause DCM that progressed to heart failure, recapitulating a crucial aspect of human *LMNA*-related DCM.

Lamin A/C reduction in cardiomyocytes activates inflammation-related transcription

To identify the onset of molecular changes preceding the functional decline of *Lmna^CKO^* hearts, we profiled the transcriptome of the heart at days 7, 11, and 14 post-tamoxifen by RNA-seq (Table S1). At days 7 and 11, *Lmna^CKO^* heart transcriptomes were almost identical to wild-type heart transcriptomes (Figure 1G). However, at day 14, *Lmna^CKO^* hearts exhibited strong transcriptional upregulation (1,751 genes) and modest downregulation (351 genes) (Figure 1G). The upregulated genes were highly overrepresented for Gene Ontology (GO) terms related to inflammatory responses (Figure 1H). These upregulated genes included innate immune-related genes such as *Cxcl10*, *Ifit1*, and *Irf7* (Figure 1I), which can be activated by the cGAS-STING pathway. The downregulated genes were overrepresented for gene pathways for cardiomyocyte metabolism and function (Figure 1H).

We examined whether the upregulation of inflammation-related genes reflected an inflammatory response in *Lmna^CKO^* hearts. We observed that the CD45^+^CD68^+^ macrophage population increased in *Lmna^CKO^* hearts at 2 weeks post-tamoxifen (Figures 1J and S1E). We also observed increased interstitial collagen deposition at 2 weeks, which developed into extensive fibrosis by 3.5 weeks post-tamoxifen (Figure 1K). Thus, Lamin A/C reduction in cardiomyocytes resulted in extensive upregulation of inflammation-related genes, macrophage expansion, and the initial fibrotic response at 2 weeks post-tamoxifen, preceding the morphological and functional changes reflective of clinical DCM (Figure 1L).

*Lmna^CKO^* cardiomyocytes develop pervasive localized nuclear envelope (NE) ruptures

We examined whether Lamin A/C reduction caused NE ruptures in cardiomyocytes. Strikingly, we observed protrusion of DNA from nuclei inside the cardiomyocytes in *Lmna^CKO^* heart sections at 2 weeks post-tamoxifen, while this event was absent in wild-type hearts (Figure 2A; of note, 90% of cardiomyocytes are binucleated in adult mice[56]). Nuclei with protruded DNA were positive for Lamin A/C staining, indicating that partial reduction of Lamin A/C was sufficient to cause DNA protrusion (Figure 2A). Electron microscopy revealed a strong condensation of protruded DNA that appeared devoid of the surrounding nuclear membrane, suggesting NE ruptures (Figures 2B and S2A). We isolated cardiomyocytes from hearts at 2 weeks post-tamoxifen, immediately fixed them, and examined the nucleus. Lamin A/C signals were specifically lost at the tips of nuclei from which DNA protruded in *Lmna^CKO^* cardiomyocytes (Figure 2C). The Lamin A/C-lost locations also lost staining for PCM1, a perinuclear matrix protein localized at the cytoplasmic side of the outer nuclear membrane[57] (Figure 2D). The loss of Lamin A/C and PCM1 occurred specifically at the tips of the elongated nuclei positioned along the longitudinal axis of the cardiomyocytes (Figures 2A–2D and S2A). The loss of NE proteins Lamin A/C and PCM1 at the nuclear tips suggested localized NE ruptures in *Lmna^CKO^* cardiomyocytes.

To determine whether NE ruptures occurred, we examined the retention of a nucleus-localized fluorescent protein. We

(G) Volcano plot comparing RNA-seq read counts in *Lmna^CKO^* versus WT hearts. Number, upregulated or downregulated gene count. *n* = 3–7 mice/genotype.

(H) Top 10 Gene Ontology (GO) terms overrepresented among differentially expressed genes. *p* value is computed by Metascape.[54]

(I) Transcript abundance in hearts quantified by RNA-seq. TPM, normalized transcripts per million. Bar, mean. *n* = 5–7 mice/genotype. P, false discovery rate (FDR)-adjusted *p* value computed by a generalized linear model in DESeq2.[55]

(J) Immunofluorescence of heart tissue sections for CD45 (pan-leukocyte, red) and CD68 (macrophage, green). Scale bar: 20 μm.

(K) Masson's trichrome staining of heart sections. Arrow, collagen deposition. Scale bar: 20 μm.
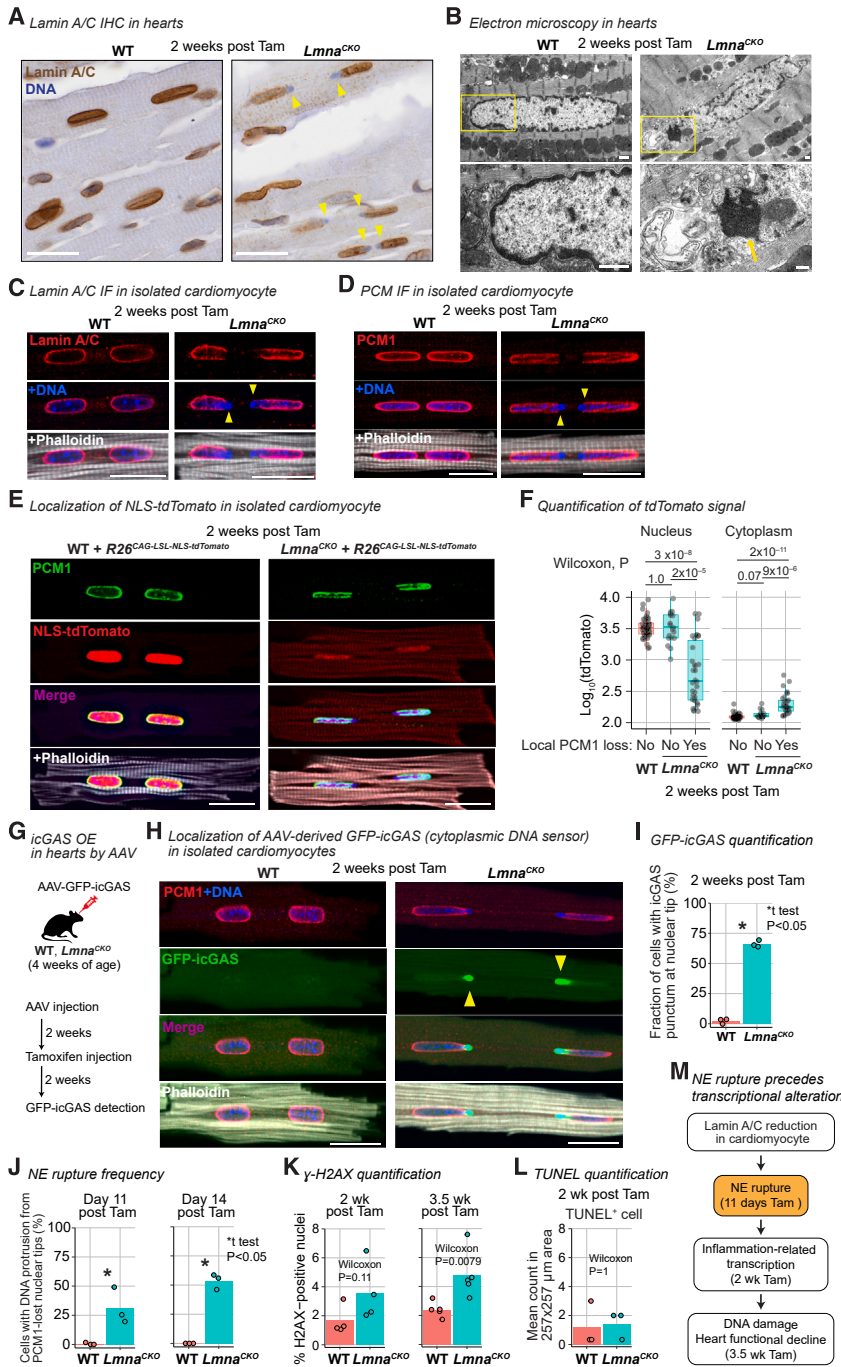
(L) Summary.

Figure 2. Lamin A/C reduction causes localized nuclear envelope rupture in cardiomyocytes

(A) Lamin A/C immunohistochemistry in heart tissue. Arrow, DNA protruded from nuclei. Scale bar: 20 μm. See Figure S2 for related analyses.

(B) Top: transmission electron micrograph of heart sections focusing on cardiomyocytes. Bottom: close-up image of the area indicated by rectangle in the top image. Arrow, protruded chromatin. Scale bar: 1 μm.

(C) Immunofluorescence for Lamin A/C in isolated cardiomyocytes. Phalloidin stains F-actin. Arrowhead, local loss of Lamin A/C with protruded DNA. Scale bar: 20 μm.

(D) Same as (C) but for PCM1 immunofluorescence.

(E) Native NLS-tdTomato signals in isolated cardiomyocytes with PCM-1 immunofluorescence. Scale bar: 20 μm.

(F) NLS-tdTomato signal intensity in nucleus and cytoplasm of cardiomyocytes (box, interquartile range). Cardiomyocytes are stratified by the presence or absence of local PCM-1 loss at the nuclear envelope. WT n = 51, $Lmna^{CKO}$ n = 53 (PCM1-loss 34, intact 19) cardiomyocytes. p value, Wilcoxon test.

(G) MyoAAV-mediated GFP-icGAS expression in cardiomyocytes *in vivo*.

(H) Native GFP-icGAS signals in isolated cardiomyocytes with PCM1 immunofluorescence. Scale bar: 20 μm.

(I) Percentage of cardiomyocytes with GFP-icGAS punctum at nuclear tip (bar, mean). n = 3 mice/genotype. p value, unpaired one-tailed Welch's t test.

(J) Percentage of cardiomyocytes with DNA protrusion from PCM1-lost nuclear tip (bar, mean). n = 3 mice/genotype. p value, same as (I).

(K) Percentage of gamma-H2AX-positive nuclei in heart section (bar, mean). n = 4–5 mice/genotype. p value, same as (F).

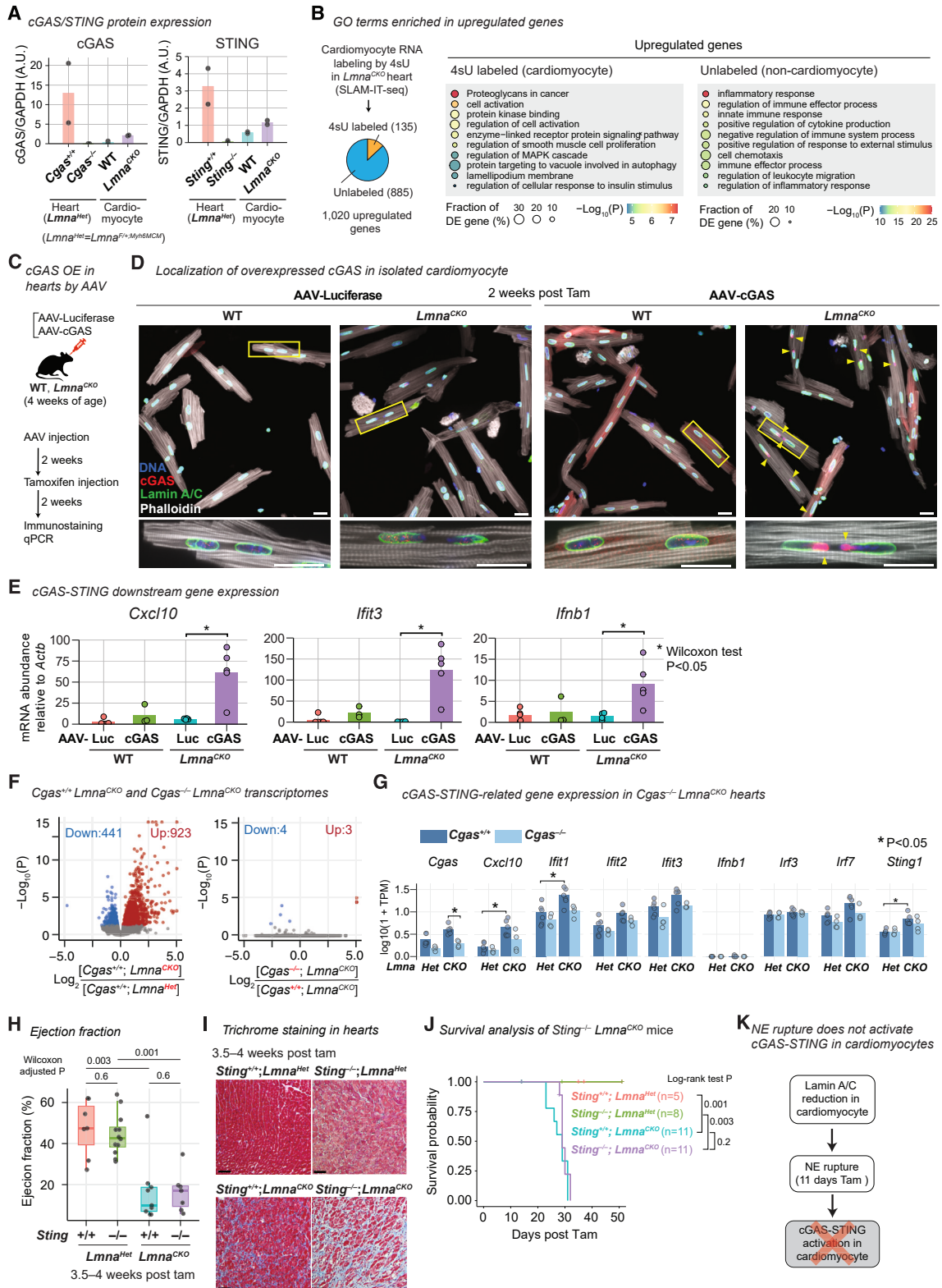(L) Number of TUNEL-positive cells in heart section (bar, mean). p value, same as (F). 3 mice/genotype.

(M) Summary.

of $Lmna^{CKO}$ cardiomyocytes with PCM1-lost nuclei. NLS-tdTomato leakage from the damaged nuclei indicated that the NE had ruptured.

To quantify NE rupture events, we expressed GFP-tagged catalytically inactive cGAS (icGAS) in cardiomyocytes *in vivo* using muscle-tropic adeno-associated virus (MyoAAV)[59] (Figure 2G). icGAS is an "NE rupture marker" owing to the cGAS's affinity to cytoplasmic DNA.[60,61] Strong icGAS punctum appeared at every PCM1-lost site on the NE in $Lmna^{CKO}$ cardiomyocytes at 2 weeks post-tamoxifen (Figures 2H and S2C). 66% of $Lmna^{CKO}$ cardiomyocytes have at least one nucleus with icGAS puncta on the NE, while such puncta were virtually absent in wild-type cardiomyocytes (Figure 2I). Thus, NE ruptures were pervasive in $Lmna^{CKO}$ cardiomyocytes at 2 weeks post-tamoxifen.

expressed nuclear localization signal (NLS)-fused tdTomato from the $Rosa26^{CAG-LSL-tdTomato}$ allele[58] in cardiomyocytes and investigated tdTomato localization at 2 weeks post-tamoxifen. NLS-tdTomato was localized exclusively to the nucleus in wild-type cardiomyocytes as well as to the intact nuclei in $Lmna^{CKO}$ cardiomyocytes (Figures 2E and S2B). However, NLS-tdTomato signals significantly diminished in nuclei with local PCM1 loss in $Lmna^{CKO}$ cardiomyocytes (Figures 2E and 2F). Reciprocally, NLS-tdTomato signals increased in the cytoplasm

A *cGAS/STING protein expression*

B *GO terms enriched in upregulated genes*

Cardiomyocyte RNA labeling by 4sU in *Lmna^CKO* heart (SLAM-IT-seq)

4sU labeled (135)
Unlabeled (885)
1,020 upregulated genes

Upregulated genes

4sU labeled (cardiomyocyte)
- Proteoglycans in cancer
- cell activation
- protein kinase binding
- regulation of cell activation
- enzyme−linked receptor protein signaling pathway
- regulation of smooth muscle cell proliferation
- regulation of MAPK cascade
- protein targeting to vacuole involved in autophagy
- lamellipodium membrane
- regulation of cellular response to insulin stimulus

Unlabeled (non-cardiomyocyte)
- inflammatory response
- regulation of immune effector process
- innate immune response
- positive regulation of cytokine production
- negative regulation of immune system process
- positive regulation of response to external stimulus
- cell chemotaxis
- immune effector process
- regulation of leukocyte migration
- regulation of inflammatory response

C *cGAS OE in hearts by AAV*

AAV-Luciferase
AAV-cGAS

WT, *Lmna^CKO* (4 weeks of age)

AAV injection
↓ 2 weeks
Tamoxifen injection
↓ 2 weeks
Immunostaining
qPCR

D *Localization of overexpressed cGAS in isolated cardiomyocyte*

2 weeks post Tam

DNA
cGAS
Lamin A/C
Phalloidin

E *cGAS-STING downstream gene expression*

* Wilcoxon test P<0.05

F *Cgas^+/+ Lmna^CKO and Cgas^−/− Lmna^CKO transcriptomes*

G *cGAS-STING-related gene expression in Cgas^−/− Lmna^CKO hearts*

* P<0.05

H *Ejection fraction*

I *Trichrome staining in hearts*
3.5–4 weeks post tam

J *Survival analysis of Sting^−/− Lmna^CKO mice*

Log-rank test P
Sting^+/+; Lmna^Het (n=5)
Sting^−/−; Lmna^Het (n=8)
Sting^+/+; Lmna^CKO (n=11)
Sting^−/−; Lmna^CKO (n=11)

K *NE rupture does not activate cGAS-STING in cardiomyocytes*

Lamin A/C reduction in cardiomyocyte
↓
NE rupture (11 days Tam)
↓
cGAS-STING activation in cardiomyocyte

(legend on next page)

To determine whether NE ruptures preceded the transcriptional change, we quantified NE ruptures at day 11 post-tamoxifen, when no transcriptional change was detected (Figure 1G). We used a local PCM1 loss with concomitant cytoplasmic DNA protrusion as a proxy for NE ruptures, as this feature strongly correlated with icGAS localization. At day 11, 31% of *Lmna^CKO* cardiomyocytes had at least one ruptured nucleus (Figures 2J, S2D, and S2E). At day 14, this frequency increased to 54%, which was comparable to 66% based on the sensitive icGAS-based quantification (Figure 2J). Thus, about one-third of *Lmna^CKO* cardiomyocytes developed NE ruptures as early as day 11 post-tamoxifen, preceding the earliest transcriptional changes, with more than 50% of cells presenting ruptures by day 14.

We investigated whether the pervasive NE ruptures in *Lmna^CKO* cardiomyocytes accompanied DNA damage accumulation. We did not find a statistically significant increase of gamma-H2AX-positive nuclei indicative of DNA double-strand breaks in *Lmna^CKO* hearts at 2 weeks post-tamoxifen (Figures 2K and S2F). In addition, there was no indication of increased cell death at this time point (Figures 2L and S2G). However, at 3.5 weeks post-tamoxifen, gamma-H2AX-positive nuclei significantly increased. Thus, pervasive NE ruptures did not cause immediate DNA damage accumulation or cell death at the time of strong inflammation-related transcriptional upregulation. Instead, DNA damage accumulated when the heart structure and function began to deteriorate (Figure 2M).

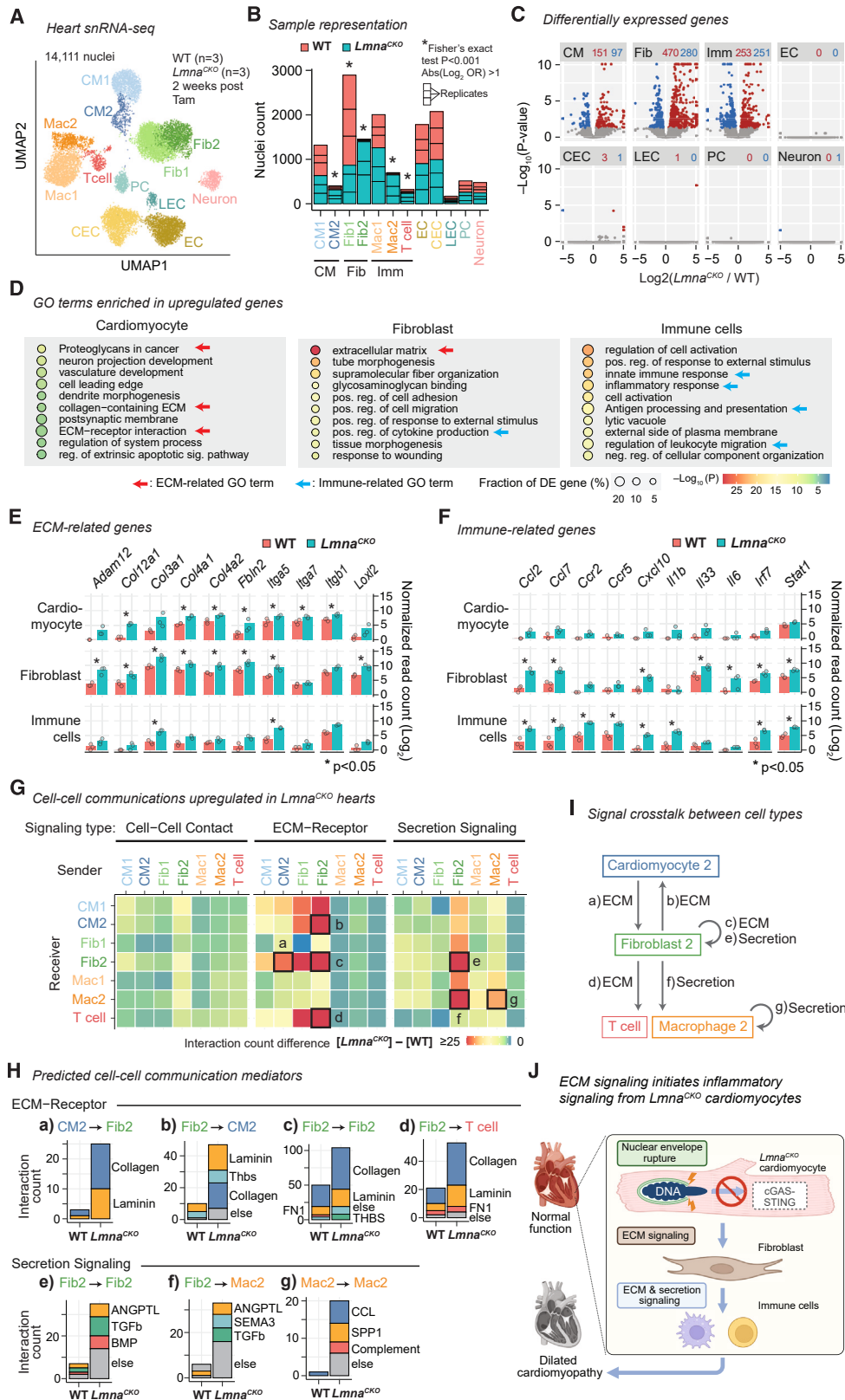### *Lmna^CKO* cardiomyocytes do not activate cGAS-STING-related transcription

Given the pervasive NE ruptures, we examined whether the cGAS-STING cytosolic DNA-sensing pathway was activated within *Lmna^CKO* cardiomyocytes. In the cGAS-STING pathway, cGAS detection of cytoplasmic DNA activates STING-mediated interferon transcription within cells bearing the cytoplasmic DNA.[46,47] This pathway has been implicated in Lamin A/C-based cardiomyopathy in a previous study.[27] We observed cGAS and STING protein expression in the heart, but interestingly, their expression within cardiomyocytes was very low in both wild-type and *Lmna^CKO* backgrounds, by immunoblots (Figures 3A, S3A, and S3B). To test whether cGAS-STING-downstream genes were upregulated within cardiomyocytes of *Lmna^CKO*

hearts, we distinguished cardiomyocyte and non-cardiomyocyte transcriptomes in hearts using SLAM-IT-seq.[62] SLAM-IT-seq labels transcripts in *Cre*-positive cardiomyocytes with 4-thiouracil (4sU) and leaves non-cardiomyocyte transcripts unlabeled (Figure S3C). As expected, cardiomyocyte-specific genes were specifically 4sU labeled in wild-type hearts (Figure S3D). We then assessed the labeling state of the 1,020 upregulated genes in *Lmna^CKO* hearts and found that 135 genes were 4sU labeled (i.e., cardiomyocyte derived) and 885 genes were not 4sU labeled (i.e., non-cardiomyocyte derived) in *Lmna^CKO* hearts at 2 weeks post-tamoxifen (Figure 3B). The cardiomyocyte-originated upregulated genes were not overrepresented for inflammation-related GO terms and did not include cGAS-STING downstream genes (Figures 3B and S3E; Table S2). Instead, they were overrepresented for the ECM-related GO terms such as "proteoglycans in cancer." On the other hand, non-cardiomyocyte-originated upregulated transcripts were enriched for inflammation-related GO terms. These data suggested that the cGAS-STING pathway was not activated within *Lmna^CKO* cardiomyocytes and that the inflammation-related transcriptional activation originated from non-cardiomyocytes in *Lmna^CKO* hearts.

We hypothesized that the near absence of cGAS expression prevented cGAS-STING activation within *Lmna^CKO* cardiomyocytes. We tested this hypothesis by overexpressing wild-type cGAS in cardiomyocytes *in vivo* with MyoAAV (Figure 3C). Without cGAS overexpression, endogenous cGAS was undetectable at NE rupture sites (Figure 3D), and the well-established cGAS-STING downstream genes *Cxcl10*, *Ifit3*, and *Ifnb1*[63–66] were transcriptionally silent in *Lmna^CKO* cardiomyocytes (Figure 3E). However, cGAS overexpression resulted in strong cGAS accumulation at NE rupture sites (Figure 3D) and strong upregulation of *Cxcl10* (10-fold), *Ifit3* (128-fold), and *Ifnb1* (6-fold) in *Lmna^CKO* cardiomyocytes (Figure 3E). In wild-type mice, cGAS overexpression did not upregulate cGAS-downstream genes, confirming the NE-rupture dependency of cGAS-downstream activation upon cGAS overexpression. Taken together, these data suggested that *Lmna^CKO* cardiomyocytes did not activate the cGAS-STING pathway despite pervasive NE ruptures, likely due to the low cGAS expression in adult cardiomyocytes.

Figure 3. cGAS and STING are not required for inflammation-related gene expression and DCM in *Lmna^CKO* mice

(A) Normalized cGAS and STING abundance quantified by immunoblot shown in Figures S3A and S3B (bar, mean). *n* = 2 mice/genotype.

(B) Left: classification of upregulated genes in *Lmna^CKO* hearts at 2 weeks post-tamoxifen into cardiomyocyte-derived or non-cardiomyocyte-derived genes based on 4sU labeling in SLAM-IT-seq (*n* = 3–8 mice/genotype). Right: top 10 GO terms overrepresented in each class of upregulated genes. *p* value is computed by Metascape.[54]

(C) MyoAAV-mediated cGAS overexpression in cardiomyocytes *in vivo*.

(D) Top: anti-cGAS and Lamin A/C immunofluorescence in isolated cardiomyocytes. Bottom: close-up image of the area indicated by rectangle in the top image. Arrowhead, cGAS at nuclear tip. Scale bar: 20 μm.

(E) Transcript abundance in isolated cardiomyocytes normalized by *Actb* abundance quantified by quantitative PCR. Bar, mean. *n* = 3–5 mice/genotype. *p* value, Wilcoxon test.

(F) Volcano plot comparing RNA-seq read counts. Left: *Cgas^+/+*;*Lmna^CKO* (*n* = 6) versus *Cgas^+/+*;*Lmna^Het* (*n* = 6). Right: *Cgas^−/−*;*Lmna^CKO* (*n* = 4) versus *Cgas^+/+*;*Lmna^CKO* (*n* = 6).

(G) Transcript abundance quantified by RNA-seq. Bar, mean. P, FDR-adjusted *p* value computed by a generalized linear model in DESeq2.[55]

(H) Left ventricular ejection fraction measured by echocardiography (box, interquartile range). *n* = 6–12 mice/genotype. *p* value, same as (E).

(I) Masson's trichrome staining of heart sections. Scale bar: 20 μm.

(J) Kaplan-Meier survival analysis. *n* = 5–11 mice/genotype. *p* value, log-rank test.

(K) Summary.

A *Heart snRNA-seq*

B *Sample representation*

C *Differentially expressed genes*

D *GO terms enriched in upregulated genes*

E *ECM-related genes*

F *Immune-related genes*

G *Cell-cell communications upregulated in Lmna^CKO hearts*

I *Signal crosstalk between cell types*

H *Predicted cell-cell communication mediators*

J *ECM signaling initiates inflammatory signaling from Lmna^CKO cardiomyocytes*

Cgas and *Sting* are not required for inflammation-related transcription and DCM in *Lmna^CKO* mice

We examined the genetic requirement of *Cgas* and *Sting*, the essential mediators of the cGAS-STING pathway, for the inflammation-related transcriptional activation and DCM in *Lmna^CKO* hearts. We validated the germline *Cgas^−/−* allele[67] crossed into *Lmna^CKO* mice or control *Lmna^Het* mice (*Lmna^F/+;Myh6Mer-CreMer*) (Figure S3A) and performed RNA-seq in hearts at 2 weeks post-tamoxifen. We first confirmed the expected strong upregulation of inflammation-related genes in *Cgas^+/+;Lmna^CKO* hearts relative to *Cgas^+/+;Lmna^Het* hearts (Figures 3F and S3F; Table S1). We then compared *Cgas^−/−;Lmna^CKO* hearts with *Cgas^+/+;Lmna^CKO* hearts. There was almost no difference in gene expression (Figure 3F), including representative cGAS-STING-downstream genes (Figures 3G and S3G), between them. These data suggested that the inflammation-related transcription in *Lmna^CKO* hearts was independent of cGAS.

We next combined germline *Sting^−/−* mice[68] with *Lmna^CKO* mice (Figure S3B) and investigated the heart phenotype. By 3.5 to 4 weeks post-tamoxifen, *Sting^−/−;Lmna^CKO* mice exhibited a reduction of ejection fraction (Figure 3H) and fibrosis (Figure 3I) as severely as the littermate control *Sting^+/+;Lmna^CKO* mice. Likewise, *Cgas^−/−;Lmna^CKO* hearts developed severe fibrosis (Figure S3H). Moreover, both *Sting^−/−;Lmna^CKO* mice and *Cgas^−/−;Lmna^CKO* mice died as early as *Sting^+/+;Lmna^CKO* or *Cgas^+/+;Lmna^CKO* mice (Figures 3J and S3I). *Sting^−/−;Lmna^Het* and *Cgas^−/−;Lmna^Het* mice maintained normal hearts and remained healthy. Taken together, our data suggested that the cGAS-STING pathway did not mediate inflammatory transcription and the pathophysiologic features of DCM in *Lmna^CKO* hearts (Figure 3K).

Cardiomyocytes, fibroblasts, and immune cells are transcriptionally altered in *Lmna^CKO* hearts

We explored alternative mechanisms by which Lamin A/C reduction in cardiomyocytes caused DCM. To identify intercellular signaling initiated by *Lmna^CKO* cardiomyocytes, we defined the cell-type-resolved transcriptional changes using single-nucleus (sn) RNA-seq (Table S3). We obtained transcriptomes for 14,111 nuclei from either wild-type or *Lmna^CKO* hearts at 2 weeks post-tamoxifen (*n* = 3; Figure 4A). These nuclei were grouped into cardiomyocytes (CM1 and CM2), fibroblasts (Fib1 and Fib2), macrophages (Mac1 and Mac2), T cells, endothelial cells (coronary, lymphatic, and other), pericytes, or neurons, based

on their transcriptomes (Figure S4A). Among these, CM2, Fib2, Mac2, and T cells were highly overrepresented by *Lmna^CKO* heart-derived cells (Figures 4B and S4B). CM2 were characterized by high *Rtn4* expression, a feature also reported in *Lmna*-KO myotubes[69] and Lamin A/C-independent heart disease[70–73] (Figure S4A). Fib2 were characterized by myofibroblast marker *Postn*,[74] Mac2 by circulating monocytic receptor *Ccr2*,[75] and T cells by T cell adaptor *Skap1*.[76] We found extensive differential gene expression within cardiomyocytes (CM1 and CM2 combined), fibroblasts (Fib1 and Fib2 combined), and immune cells (Mac1, Mac2, and T cells combined), while other cell types exhibited almost no expression differences (Figures 4C, 4D, and S4C; Table S4). The upregulated genes in cardiomyocytes were not overrepresented for the cytosolic DNA-sensing pathway and did not include cell-death-related genes but did include some DNA-damage-repair-related genes, as expected (Figures S4D–S4F).

Interestingly, upregulated genes in *Lmna^CKO* cardiomyocytes and those in fibroblasts were both most strongly overrepresented for ECM-related pathways (Figure 4D). The upregulated ECM-related genes included collagen and integrin genes (in cardiomyocytes and fibroblasts), and ECM proteinase and cross-linker genes (specifically in fibroblasts) (Figure 4E). On the other hand, fibroblasts and immune cells, but not cardiomyocytes, commonly upregulated immune-related genes including cytokine, cytokine receptor, and cytokine transcription factor genes (Figures 4D and F). These results suggested potential signal crosstalk between cardiomyocytes and fibroblasts and between fibroblasts and immune cells in *Lmna^CKO* hearts.

ECM-mediated signaling from *Lmna^CKO* cardiomyocytes is predicted to activate fibroblasts

We investigated intercellular signal crosstalk in *Lmna^CKO* hearts by applying the CellChat program[77] to the snRNA-seq data. This analysis predicted ECM-receptor signaling from CM2 to Fib2 as the only strongly upregulated signaling originating from CM2, the population predominantly consisting of *Lmna^CKO* cardiomyocyte nuclei (Figure 4G, box a). Collagens and laminins were predicted to mediate this CM2-to-Fib2 signaling (Figure 4H). CM2 were not predicted to signal directly to immune cell populations. Instead, Fib2 were predicted to send ECM-mediated signals to CM2 (box b), Fib2 (box c), and T cells (box d) via collagens, laminins, thrombospondins, and fibronectins (Figures 4G and 4H). Fib2 were also predicted to send secretion-mediated signals to Fib2 (box

Figure 4. ECM-mediated signaling from *Lmna^CKO* cardiomyocytes is predicted to activate fibroblasts
(A) snRNA-seq uniform manifold approximation and projection (UMAP) plot for WT and *Lmna^CKO* heart nuclei. CM, cardiomyocyte; Fib, fibroblast; Mac, macrophage; EC, endothelial cell; CEC, coronary EC; LEC, lymphatic EC; PC, pericyte. See Figure S4 for additional analyses.
(B) WT and *Lmna^CKO* nucleus count within each cell type cluster. Cell types combined in later analyses are indicated below the graph.
(C) snRNA-seq pseudo-bulk volcano plot comparing *Lmna^CKO* versus WT heart nuclei. Red, upregulated genes. Blue, downregulated genes. The number of differentially expressed genes is indicated above the plot.
(D) GO terms enriched among upregulated genes within indicated cell type. *p* value is computed by Metascape.[54]
(E) Pseudo-bulk transcript abundance of ECM-related genes. Point, mean of normalized read count per replicate. Bar, mean across replicates. P, FDR-adjusted *p* value computed by a generalized linear model in DESeq2.[55]
(F) Same as (E) but for immune-related genes.
(G) Predicted signaling from sender cells (x axis) to receiver cells (y axis). Color: signaling gains in *Lmna^CKO* hearts relative to WT hearts.
(H) Predicted signaling mediators for the signaling indicated by box in (G) with alphabetical labels.
(I) Predicted intercellular signaling indicated in (G) by alphabetical labels in *Lmna^CKO* hearts.
(J) Model.

e) and Mac2 (box f) via ANGPTL (angiopoietin-like), transforming growth factor beta, BMP, and SEMA3 (semaphorin3). Fib2 might therefore act as a central signaling hub in *Lmna*^{CKO} hearts, receiving signals from CM2 and sending signals to immune cells (Figure 4I). Finally, Mac2 were predicted to send secretion-mediated signals to Mac2 themselves (box g) via CCL (chemokine ligands), SPP1 (osteopontins), and complement factors. This signaling might mediate the macrophage infiltration observed in *Lmna*^{CKO} hearts (Figure 1J). Taken together, our results suggested that *Lmna*^{CKO} cardiomyocytes activated fibroblasts via ECM-mediated signaling, not cytokine-mediated signaling such as cGAS-STING, and that fibroblasts activated and recruited immune cells through both ECM signaling and secretion signaling to orchestrate inflammatory signaling in the heart (Figure 4J).

DISCUSSION

We report that frequent localized NE ruptures precede transcriptional changes, DNA damage accumulation, and heart functional decline in *Lmna*^{CKO} hearts. Given our observation that a 50% reduction of Lamin A/C proteins is sufficient to induce pervasive NE ruptures in cardiomyocytes, NE ruptures might be more prevalent than previously anticipated in patients with *LMNA*-related DCM. NE ruptures might have been overlooked due to the specific location of localized NE ruptures at the tips of elongated nuclei within cardiomyocytes. The mechanisms underlying NE ruptures and the causal role of NE ruptures in DCM remain to be investigated.

Our data indicate that the cGAS-STING pathway does not contribute to *LMNA*-related DCM in the adult mouse model investigated herein. This suggests that pharmacologically reducing cGAS-STING activity for treating *LMNA*-related DCM, an idea previously discussed,[27,78] may be ineffective. Our conclusion diverges from a previous report that *Cgas* deletion can delay early post-natal cardiomyopathy caused by *Lmna* deletion in embryonic hearts.[27] This difference may be due to the near absence of cGAS expression preventing cGAS-STING activation in adult cardiomyocytes, whereas the basal cGAS-STING activity may be higher in early post-natal cardiomyocytes.[79,80] The lack of robust cGAS expression may reduce pathogen-derived DNA sensing in adult cardiomyocytes, similar to hepatocytes that also lack functional cGAS-STING.[81] Many reports suggest an association between DNA damage and cGAS-STING activation.[27,82–85] Our data that *Lmna*^{CKO} cardiomyocytes accumulate DNA damage without activating cGAS-STING suggest that DNA damage and cGAS-STING can be uncoupled.

Our study nominates ECM signaling as a mechanism by which Lamin A/C-reduced cardiomyocytes initiate an inflammatory response by activating fibroblasts. A recent study reported a similar observation in which NE rupture induces ECM remodeling through unknown mechanisms that require DNA damage.[86] Further study on the potential roles of ECM signaling in *LMNA*-related DCM is required.

Limitations of the study

We reduced Lamin A/C exclusively within the cardiomyocytes of adult mice. Whether Lamin A/C reduction in other cell types or at other stages causes NE ruptures and contributes to DCM through cGAS-STING activation remains an open question.

STAR★METHODS

Detailed methods are provided in the online version of this paper and include the following:

- KEY RESOURCES TABLE
- RESOURCE AVAILABILITY
  - Lead contact
  - Materials availability
  - Data and code availability
- EXPERIMENTAL MODEL AND STUDY PARTICIPANT DETAILS
  - Mouse genetics and treatment
- METHOD DETAILS
  - Mouse genotyping
  - Echocardiography
  - Survival analysis
  - Histological staining
  - Cardiomyocyte isolation
  - Immunohistochemistry
  - Immunofluorescence on tissue sections
  - Immunofluorescence on isolated cardiomyocytes
  - Plasmid construction
  - MyoAAV production and *in vivo* transduction
  - Image quantification related to nuclear envelope ruptures
  - TUNEL assay
  - Immunoblot
  - Electron microscopy
  - Quantitative reverse-transcriptase PCR (RT-PCR)
  - RNA-seq
  - RNA-seq analysis
  - Single-nucleus RNA-seq
  - Single-nucleus RNA-seq analysis
  - SLAM-IT-seq
  - SLAM-IT-seq analysis
- QUANTIFICATION AND STATISTICAL ANALYSIS

SUPPLEMENTAL INFORMATION

Supplemental information can be found online at https://doi.org/10.1016/j.celrep.2024.114284.

AUTHOR CONTRIBUTIONS

Conceptualization, A.E. and K.I.; methodology, A.E., I.P.M., and K.I.; formal analysis, A.E. and K.I.; investigation, A.E., H.B., B.T., A.S., S.I., B.L., O.A., P.P., and K.I.; resources, I.P.M.; data curation, A.E. and K.I.; writing – original draft, A.E. and K.I.; writing – review & editing, A.E., I.P.M., and K.I.; visualization, A.E. and K.I.; supervision, K.I.; project administration, K.I.; funding acquisition, K.I. and I.P.M.

DECLARATION OF INTERESTS

The authors declare no competing interests.

REFERENCES

1. Aebi, U., Cohn, J., Buhle, L., and Gerace, L. (1986). The nuclear lamina is a meshwork of intermediate-type filaments. Nature *323*, 560–564.

2. Goldman, A.E., Maul, G., Steinert, P.M., Yang, H.Y., and Goldman, R.D. (1986). Keratin-like proteins that coisolate with intermediate filaments of BHK-21 cells are nuclear lamins. Proc. Natl. Acad. Sci. USA *83*, 3839–3843.

3. Röber, R.A., Weber, K., and Osborn, M. (1989). Differential timing of nuclear lamin A/C expression in the various organs of the mouse embryo and the young animal: a developmental study. Development *105*, 365–378.

4. Dechat, T., Pfleghaar, K., Sengupta, K., Shimi, T., Shumaker, D.K., Solimando, L., and Goldman, R.D. (2008). Nuclear lamins: major factors in the structural organization and function of the nucleus and chromatin. Genes Dev. *22*, 832–853.

5. Fatkin, D., MacRae, C., Sasaki, T., Wolff, M.R., Porcu, M., Frenneaux, M., Atherton, J., Vidaillet, H.J., Jr., Spudich, S., De Girolami, U., et al. (1999). Missense mutations in the rod domain of the lamin A/C gene as causes of dilated cardiomyopathy and conduction-system disease. N. Engl. J. Med. *341*, 1715–1724.

6. Bonne, G., Di Barletta, M.R., Varnous, S., Bécane, H.M., Hammouda, E.H., Merlini, L., Muntoni, F., Greenberg, C.R., Gary, F., Urtizberea, J.A., et al. (1999). Mutations in the gene encoding lamin A/C cause autosomal dominant Emery-Dreifuss muscular dystrophy. Nat. Genet. *21*, 285–288.

7. Eriksson, M., Brown, W.T., Gordon, L.B., Glynn, M.W., Singer, J., Scott, L., Erdos, M.R., Robbins, C.M., Moses, T.Y., Berglund, P., et al. (2003). Recurrent de novo point mutations in lamin A cause Hutchinson-Gilford progeria syndrome. Nature *423*, 293–298.

8. Chen, L., Lee, L., Kudlow, B.A., Dos Santos, H.G., Sletvold, O., Shafeghati, Y., Botha, E.G., Garg, A., Hanson, N.B., Martin, G.M., et al. (2003). LMNA mutations in atypical Werner's syndrome. Lancet *362*, 440–445.

9. De Sandre-Giovannoli, A., Bernard, R., Cau, P., Navarro, C., Amiel, J., Boccaccio, I., Lyonnet, S., Stewart, C.L., Munnich, A., Le Merrer, M., and Lévy, N. (2003). Lamin a truncation in Hutchinson-Gilford progeria. Science *300*, 2055.

10. Cao, H., and Hegele, R.A. (2000). Nuclear lamin A/C R482Q mutation in canadian kindreds with Dunnigan-type familial partial lipodystrophy. Hum. Mol. Genet. *9*, 109–112.

11. Parks, S.B., Kushner, J.D., Nauman, D., Burgess, D., Ludwigsen, S., Peterson, A., Li, D., Jakobs, P., Litt, M., Porter, C.B., et al. (2008). Lamin A/C mutation analysis in a cohort of 324 unrelated patients with idiopathic or familial dilated cardiomyopathy. Am. Heart J. *156*, 161–169.

12. Hershberger, R.E., and Morales, A. (2008). LMNA-Related Dilated Cardiomyopathy. In GeneReviews®, M.P. Adam, H.H. Ardinger, R.A. Pagon, S.E. Wallace, L.J.H. Bean, K. Stephens, and A. Amemiya, eds. (University of Washington, Seattle).

13. Taylor, M.R.G., Fain, P.R., Sinagra, G., Robinson, M.L., Robertson, A.D., Carniel, E., Di Lenarda, A., Bohlmeyer, T.J., Ferguson, D.A., Brodsky, G.L., et al. (2003). Natural history of dilated cardiomyopathy due to lamin A/C gene mutations. J. Am. Coll. Cardiol. *41*, 771–780.

14. Sébillon, P., Bouchier, C., Bidot, L.D., Bonne, G., Ahamed, K., Charron, P., Drouin-Garraud, V., Millaire, A., Desrumeaux, G., Benaïche, A., et al. (2003). Expanding the phenotype of LMNA mutations in dilated cardiomyopathy and functional consequences of these mutations. J. Med. Genet. *40*, 560–567.

15. van Rijsingen, I.A.W., Nannenberg, E.A., Arbustini, E., Elliott, P.M., Mogensen, J., Hermans-van Ast, J.F., van der Kooi, A.J., van Tintelen, J.P., van den Berg, M.P., Grasso, M., et al. (2013). Gender-specific differences in major cardiac events and mortality in lamin A/C mutation carriers. Eur. J. Heart Fail. *15*, 376–384.

16. Charron, P., Arbustini, E., and Bonne, G. (2012). What Should the Cardiologist know about Lamin Disease? Arrhythm. Electrophysiol. Rev. *1*, 22–28.

17. Verga, L., Concardi, M., Pilotto, A., Bellini, O., Pasotti, M., Repetto, A., Tavazzi, L., and Arbustini, E. (2003). Loss of lamin A/C expression revealed by immuno-electron microscopy in dilated cardiomyopathy with atrioventricular block caused by LMNA gene defects. Virchows Arch. *443*, 664–671.

18. Arbustini, E., Pilotto, A., Repetto, A., Grasso, M., Negri, A., Diegoli, M., Campana, C., Scelsi, L., Baldini, E., Gavazzi, A., and Tavazzi, L. (2002). Autosomal dominant dilated cardiomyopathy with atrioventricular block: a lamin A/C defect-related disease. J. Am. Coll. Cardiol. *39*, 981–990.

19. Kato, K., Ohno, S., Sonoda, K., Makiyama, T., Ozawa, T., and Horie, M. (2020). Splice site mutation of LMNA causes severe dilated cardiomyopathy via strong dominant reduction of total lamin expression. Eur. Heart J. *41*. https://doi.org/10.1093/ehjci/ehaa946.0333.

20. Narula, N., Favalli, V., Tarantino, P., Grasso, M., Pilotto, A., Bellazzi, R., Serio, A., Gambarin, F.I., Charron, P., Meder, B., et al. (2012). Quantitative expression of the mutated lamin A/C gene in patients with cardiolaminopathy. J. Am. Coll. Cardiol. *60*, 1916–1920.

21. Muchir, A., Pavlidis, P., Decostre, V., Herron, A.J., Arimura, T., Bonne, G., and Worman, H.J. (2007). Activation of MAPK pathways links LMNA mutations to cardiomyopathy in Emery-Dreifuss muscular dystrophy. J. Clin. Invest. *117*, 1282–1293.

22. Muchir, A., Shan, J., Bonne, G., Lehnart, S.E., and Worman, H.J. (2009). Inhibition of extracellular signal-regulated kinase signaling to prevent cardiomyopathy caused by mutation in the gene encoding A-type lamins. Hum. Mol. Genet. *18*, 241–247.

23. Wu, W., Muchir, A., Shan, J., Bonne, G., and Worman, H.J. (2011). Mitogen-Activated Protein Kinase Inhibitors Improve Heart Function and Prevent Fibrosis in Cardiomyopathy Caused by Mutation in Lamin A/C Gene. Circulation *123*, 53–61.

24. Muchir, A., Wu, W., Choi, J.C., Iwata, S., Morrow, J., Homma, S., and Worman, H.J. (2012). Abnormal p38α mitogen-activated protein kinase signaling in dilated cardiomyopathy caused by lamin A/C gene mutation. Hum. Mol. Genet. *21*, 4325–4333.

25. Choi, J.C., Muchir, A., Wu, W., Iwata, S., Homma, S., Morrow, J.P., and Worman, H.J. (2012). Temsirolimus activates autophagy and ameliorates cardiomyopathy caused by lamin A/C gene mutation. Sci. Transl. Med. *4*, 144ra102.

26. Chen, S.N., Lombardi, R., Karmouch, J., Tsai, J.-Y., Czernuszewicz, G., Taylor, M.R.G., Mestroni, L., Coarfa, C., Gurha, P., and Marian, A.J. (2019). DNA Damage Response/TP53 Pathway Is Activated and Contributes to the Pathogenesis of Dilated Cardiomyopathy Associated With LMNA (Lamin A/C) Mutations. Circ. Res. *124*, 856–873.

27. Cheedipudi, S.M., Asghar, S., and Marian, A.J. (2022). Genetic Ablation of the DNA Damage Response Pathway Attenuates Lamin-Associated Dilated Cardiomyopathy in Mice. JACC. Basic Transl. Sci. *7*, 1232–1245.

28. Davidson, P.M., and Lammerding, J. (2014). Broken nuclei–lamins, nuclear mechanics, and disease. Trends Cell Biol. *24*, 247–256.

29. Chen, N.Y., Yang, Y., Weston, T.A., Belling, J.N., Heizer, P., Tu, Y., Kim, P., Edillo, L., Jonas, S.J., Weiss, P.S., et al. (2019). An absence of lamin B1 in migrating neurons causes nuclear membrane ruptures and cell death. Proc. Natl. Acad. Sci. USA *116*, 25870–25879.

30. Cho, S., Vashisth, M., Abbas, A., Majkut, S., Vogel, K., Xia, Y., Ivanovska, I.L., Irianto, J., Tewari, M., Zhu, K., et al. (2019). Mechanosensing by the Lamina Protects against Nuclear Rupture, DNA Damage, and Cell-Cycle Arrest. Dev. Cell *49*, 920–935.e5.

31. Earle, A.J., Kirby, T.J., Fedorchak, G.R., Isermann, P., Patel, J., Iruvanti, S., Moore, S.A., Bonne, G., Wallrath, L.L., and Lammerding, J. (2020). Mutant lamins cause nuclear envelope rupture and DNA damage in skeletal muscle cells. Nat. Mater. *19*, 464–473.

32. Hatch, E.M., and Hetzer, M.W. (2016). Nuclear envelope rupture is induced by actin-based nucleus confinement. J. Cell Biol. *215*, 27–36.

33. Vargas, J.D., Hatch, E.M., Anderson, D.J., and Hetzer, M.W. (2012). Transient nuclear envelope rupturing during interphase in human cancer cells. Nucleus *3*, 88–100.

34. De Vos, W.H., Houben, F., Kamps, M., Malhas, A., Verheyen, F., Cox, J., Manders, E.M.M., Verstraeten, V.L.R.M., van Steensel, M.A.M., Marcelis, C.L.M., et al. (2011). Repetitive disruptions of the nuclear envelope invoke temporary loss of cellular compartmentalization in laminopathies. Hum. Mol. Genet. *20*, 4175–4186.

35. Sylvius, N., Bilinska, Z.T., Veinot, J.P., Fidzianska, A., Bolongo, P.M., Poon, S., McKeown, P., Davies, R.A., Chan, K.-L., Tang, A.S.L., et al. (2005). In vivo and in vitro examination of the functional significances of novel lamin gene mutations in heart failure patients. J. Med. Genet. *42*, 639–647.

36. Siu, C.-W., Lee, Y.-K., Ho, J.C.-Y., Lai, W.-H., Chan, Y.-C., Ng, K.-M., Wong, L.-Y., Au, K.-W., Lau, Y.-M., Zhang, J., et al. (2012). Modeling of lamin A/C mutation premature cardiac aging using patient-specific induced pluripotent stem cells. Aging *4*, 803–822.

37. Fan, Y., Tan, D., Zhang, X., Song, D., Chang, X., Wang, S., Yan, H., Ge, L., Yang, H., Bönnemann, C., et al. (2020). Nuclear Factor-κB Pathway Mediates the Molecular Pathogenesis of LMNA-Related Muscular Dystrophies. Biochem. Genet. *58*, 966–980.

38. Chai, R.J., Werner, H., Li, P.Y., Lee, Y.L., Nyein, K.T., Solovei, I., Luu, T.D.A., Sharma, B., Navasankari, R., Maric, M., et al. (2021). Disrupting the LINC complex by AAV mediated gene transduction prevents progression of Lamin induced cardiomyopathy. Nat. Commun. *12*, 4722.

39. Chen, R., Buchmann, S., Kroth, A., Arias-Loza, A.-P., Kohlhaas, M., Wagner, N., Grüner, G., Nickel, A., Cirnu, A., Williams, T., et al. (2023). Mechanistic Insights of the LEMD2 p.L13R Mutation and Its Role in Cardiomyopathy. Circ. Res. *132*, e43–e58.

40. Kim, P.H., Chen, N.Y., Heizer, P.J., Tu, Y., Weston, T.A., Fong, J.L.-C., Gill, N.K., Rowat, A.C., Young, S.G., and Fong, L.G. (2021). Nuclear membrane ruptures underlie the vascular pathology in a mouse model of Hutchinson-Gilford progeria syndrome. JCI Insight *6*, e151515. https://doi.org/10.1172/jci.insight.151515.

41. Ross, J.A., Arcos-Villacis, N., Battey, E., Boogerd, C., Orellana, C.A., Marhuenda, E., Swiatlowska, P., Hodzic, D., Prin, F., Mohun, T., et al. (2023). Lem2 is essential for cardiac development by maintaining nuclear integrity. Cardiovasc. Res. *119*, 2074–2088. https://doi.org/10.1093/cvr/cvad061.

42. Zhang, Y., Ramirez-Martinez, A., Chen, K., McAnally, J.R., Cai, C., Durbacz, M.Z., Chemello, F., Wang, Z., Xu, L., Bassel-Duby, R., et al. (2023). Net39 protects muscle nuclei from mechanical stress during the pathogenesis of Emery-Dreifuss muscular dystrophy. J. Clin. Invest. *133*, e163333. https://doi.org/10.1172/JCI163333.

43. Eissenberg, J.C., and Gonzalo, S. (2020). Pushing the limit on laminopathies. Nat. Mater. *19*, 378–380.

44. Gauthier, B.R., and Comaills, V. (2021). Nuclear Envelope Integrity in Health and Disease: Consequences on Genome Instability and Inflammation. Int. J. Mol. Sci. *22*, 7281. https://doi.org/10.3390/ijms22147281.

45. Miller, K.N., Victorelli, S.G., Salmonowicz, H., Dasgupta, N., Liu, T., Passos, J.F., and Adams, P.D. (2021). Cytoplasmic DNA: sources, sensing, and role in aging and disease. Cell *184*, 5506–5526.

46. Yum, S., Li, M., Fang, Y., and Chen, Z.J. (2021). TBK1 recruitment to STING activates both IRF3 and NF-κB that mediate immune defense against tumors and viral infections. Proc. Natl. Acad. Sci. USA *118*, e2100225118.

47. Decout, A., Katz, J.D., Venkatraman, S., and Ablasser, A. (2021). The cGAS–STING pathway as a therapeutic target in inflammatory diseases. Nat. Rev. Immunol. *21*, 548–569.

48. Kreienkamp, R., Graziano, S., Coll-Bonfill, N., Bedia-Diaz, G., Cybulla, E., Vindigni, A., Dorsett, D., Kubben, N., Batista, L.F.Z., and Gonzalo, S. (2018). A Cell-Intrinsic Interferon-like Response Links Replication Stress to Cellular Aging Caused by Progerin. Cell Rep. *22*, 2006–2015.

49. King, K.R., Aguirre, A.D., Ye, Y.-X., Sun, Y., Roh, J.D., Ng, R.P., Jr., Kohler, R.H., Arlauckas, S.P., Iwamoto, Y., Savol, A., et al. (2017). IRF3 and type I interferons fuel a fatal response to myocardial infarction. Nat. Med. *23*, 1481–1487.

50. Cao, D.J., Schiattarella, G.G., Villalobos, E., Jiang, N., May, H.I., Li, T., Chen, Z.J., Gillette, T.G., and Hill, J.A. (2018). Cytosolic DNA Sensing Promotes Macrophage Transformation and Governs Myocardial Ischemic Injury. Circulation *137*, 2613–2634.

51. Hu, D., Cui, Y.-X., Wu, M.-Y., Li, L., Su, L.-N., Lian, Z., and Chen, H. (2020). Cytosolic DNA sensor cGAS plays an essential pathogenetic role in pressure overload-induced heart failure. Am. J. Physiol. Heart Circ. Physiol. *318*, H1525–H1537.

52. Yan, M., Li, Y., Luo, Q., Zeng, W., Shao, X., Li, L., Wang, Q., Wang, D., Zhang, Y., Diao, H., et al. (2022). Mitochondrial damage and activation of the cytosolic DNA sensor cGAS-STING pathway lead to cardiac pyroptosis and hypertrophy in diabetic cardiomyopathy mice. Cell Death Discov. *8*, 258.

53. Hasper, J., Welle, K., Swovick, K., Hryhorenko, J., Ghaemmaghami, S., and Buchwalter, A. (2024). Long lifetime and tissue-specific accumulation of lamin A/C in Hutchinson-Gilford progeria syndrome. J. Cell Biol. *223*, e202307049. https://doi.org/10.1083/jcb.202307049.

54. Zhou, Y., Zhou, B., Pache, L., Chang, M., Khodabakhshi, A.H., Tanaseichuk, O., Benner, C., and Chanda, S.K. (2019). Metascape provides a biologist-oriented resource for the analysis of systems-level datasets. Nat. Commun. *10*, 1523.

55. Love, M.I., Huber, W., and Anders, S. (2014). Moderated estimation of fold change and dispersion for RNA-seq data with DESeq2. Genome Biol. *15*, 550.

56. Patterson, M., Barske, L., Van Handel, B., Rau, C.D., Gan, P., Sharma, A., Parikh, S., Denholtz, M., Huang, Y., Yamaguchi, Y., et al. (2017). Frequency of mononuclear diploid cardiomyocytes underlies natural variation in heart regeneration. Nat. Genet. *49*, 1346–1353.

57. Srsen, V., Fant, X., Heald, R., Rabouille, C., and Merdes, A. (2009). Centrosome proteins form an insoluble perinuclear matrix during muscle cell differentiation. BMC Cell Biol. *10*, 28.

58. Daigle, T.L., Madisen, L., Hage, T.A., Valley, M.T., Knoblich, U., Larsen, R.S., Takeno, M.M., Huang, L., Gu, H., Larsen, R., et al. (2018). A Suite of Transgenic Driver and Reporter Mouse Lines with Enhanced Brain-Cell-Type Targeting and Functionality. Cell *174*, 465–480.e22.

59. Tabebordbar, M., Lagerborg, K.A., Stanton, A., King, E.M., Ye, S., Tellez, L., Krunnfusz, A., Tavakoli, S., Widrick, J.J., Messemer, K.A., et al. (2021). Directed evolution of a family of AAV capsid variants enabling potent muscle-directed gene delivery across species. Cell *184*, 4919–4938.e22.

60. Denais, C.M., Gilbert, R.M., Isermann, P., McGregor, A.L., te Lindert, M., Weigelin, B., Davidson, P.M., Friedl, P., Wolf, K., and Lammerding, J. (2016). Nuclear envelope rupture and repair during cancer cell migration. Science *352*, 353–358.

61. Raab, M., Gentili, M., de Belly, H., Thiam, H.R., Vargas, P., Jimenez, A.J., Lautenschlaeger, F., Voituriez, R., Lennon-Duménil, A.M., Manel, N., and Piel, M. (2016). ESCRT III repairs nuclear envelope ruptures during cell migration to limit DNA damage and cell death. Science *352*, 359–362.

62. Matsushima, W., Herzog, V.A., Neumann, T., Gapp, K., Zuber, J., Ameres, S.L., and Miska, E.A. (2019). Sequencing cell-type-specific transcriptomes with SLAM-ITseq. Nat. Protoc. *14*, 2261–2278.

63. Kuhl, N., Linder, A., Philipp, N., Nixdorf, D., Fischer, H., Veth, S., Kuut, G., Xu, T.T., Theurich, S., Carell, T., et al. (2023). STING agonism turns

human T cells into interferon-producing cells but impedes their functionality. EMBO Rep. 24, e55536.

64. Liu, Y., Xu, P., Rivara, S., Liu, C., Ricci, J., Ren, X., Hurley, J.H., and Ablasser, A. (2022). Clathrin-associated AP-1 controls termination of STING signalling. Nature 610, 761–767.

65. Ikushima, H., Negishi, H., and Taniguchi, T. (2013). The IRF family transcription factors at the interface of innate and adaptive immune responses. Cold Spring Harb. Symp. Quant. Biol. 78, 105–116.

66. Della Corte, C.M., Sen, T., Gay, C.M., Ramkumar, K., Diao, L., Cardnell, R.J., Rodriguez, B.L., Stewart, C.A., Papadimitrakopoulou, V.A., Gibson, L., et al. (2020). STING Pathway Expression Identifies NSCLC With an Immune-Responsive Phenotype. J. Thorac. Oncol. 15, 777–791.

67. Schoggins, J.W., MacDuff, D.A., Imanaka, N., Gainey, M.D., Shrestha, B., Eitson, J.L., Mar, K.B., Richardson, R.B., Ratushny, A.V., Litvak, V., et al. (2014). Pan-viral specificity of IFN-induced genes reveals new roles for cGAS in innate immunity. Nature 505, 691–695.

68. Jin, L., Hill, K.K., Filak, H., Mogan, J., Knowles, H., Zhang, B., Perraud, A.-L., Cambier, J.C., and Lenz, L.L. (2011). MPYS is required for IFN response factor 3 activation and type I IFN production in the response of cultured phagocytes to bacterial second messengers cyclic-di-AMP and cyclic-di-GMP. J. Immunol. 187, 2595–2601.

69. Cohen, T.V., Gnocchi, V.F., Cohen, J.E., Phadke, A., Liu, H., Ellis, J.A., Foisner, R., Stewart, C.L., Zammit, P.S., and Partridge, T.A. (2013). Defective skeletal muscle growth in lamin A/C-deficient mice is rescued by loss of Lap2α. Hum. Mol. Genet. 22, 2852–2869.

70. Ortega, A., Roselló-Lletí, E., Tarazón, E., Molina-Navarro, M.M., Martínez-Dolz, L., González-Juanatey, J.R., Lago, F., Montoro-Mateos, J.D., Salvador, A., Rivera, M., and Portolés, M. (2014). Endoplasmic reticulum stress induces different molecular structural alterations in human dilated and ischemic cardiomyopathy. PLoS One 9, e107635.

71. Sasagawa, S., Nishimura, Y., Okabe, S., Murakami, S., Ashikawa, Y., Yuge, M., Kawaguchi, K., Kawase, R., Okamoto, R., Ito, M., and Tanaka, T. (2016). Downregulation of GSTK1 Is a Common Mechanism Underlying Hypertrophic Cardiomyopathy. Front. Pharmacol. 7, 162.

72. Fan, P., Zhang, L., Cheng, T., Wang, J., Zhou, J., Zhao, L., Hua, C., and Xia, Q. (2021). MiR-590-5p inhibits pathological hypertrophy mediated heart failure by targeting RTN4. J. Mol. Histol. 52, 955–964.

73. Wehrens, M., de Leeuw, A.E., Wright-Clark, M., Eding, J.E.C., Boogerd, C.J., Molenaar, B., van der Kraak, P.H., Kuster, D.W.D., van der Velden, J., Michels, M., et al. (2022). Single-cell transcriptomics provides insights into hypertrophic cardiomyopathy. Cell Rep. 39, 110809.

74. Snider, P., Standley, K.N., Wang, J., Azhar, M., Doetschman, T., and Conway, S.J. (2009). Origin of cardiac fibroblasts and the role of periostin. Circ. Res. 105, 934–947.

75. Lavine, K.J., Epelman, S., Uchida, K., Weber, K.J., Nichols, C.G., Schilling, J.D., Ornitz, D.M., Randolph, G.J., and Mann, D.L. (2014). Distinct macrophage lineages contribute to disparate patterns of cardiac recovery and remodeling in the neonatal and adult heart. Proc. Natl. Acad. Sci. USA 111, 16029–16034.

76. Liu, C., Raab, M., Gui, Y., and Rudd, C.E. (2023). Multi-functional adaptor SKAP1: regulator of integrin activation, the stop-signal, and the proliferation of T cells. Front. Immunol. 14, 1192838.

77. Jin, S., Guerrero-Juarez, C.F., Zhang, L., Chang, I., Ramos, R., Kuan, C.-H., Myung, P., Plikus, M.V., and Nie, Q. (2021). Inference and analysis of cell-cell communication using CellChat. Nat. Commun. 12, 1088.

78. Zhang, H., Ren, L., and Wu, J.C. (2022). New Insights Into the Therapy for Lamin-Associated Dilated Cardiomyopathy. JACC. Basic Transl. Sci. 7, 1246–1248.

79. Long, Z.-J., Wang, J.-D., Xu, J.-Q., Lei, X.-X., and Liu, Q. (2022). cGAS/STING cross-talks with cell cycle and potentiates cancer immunotherapy. Mol. Ther. 30, 1006–1017.

80. Yang, H., Wang, H., Ren, J., Chen, Q., and Chen, Z.J. (2017). cGAS is essential for cellular senescence. Proc. Natl. Acad. Sci. USA 114, E4612–E4620.

81. Thomsen, M.K., Nandakumar, R., Stadler, D., Malo, A., Valls, R.M., Wang, F., Reinert, L.S., Dagnaes-Hansen, F., Hollensen, A.K., Mikkelsen, J.G., et al. (2016). Lack of immunological DNA sensing in hepatocytes facilitates hepatitis B virus infection. Hepatology 64, 746–759.

82. Li, T., and Chen, Z.J. (2018). The cGAS-cGAMP-STING pathway connects DNA damage to inflammation, senescence, and cancer. J. Exp. Med. 215, 1287–1299.

83. Willaume, S., Rass, E., Fontanilla-Ramirez, P., Moussa, A., Wanschoor, P., and Bertrand, P. (2021). A Link between Replicative Stress, Lamin Proteins, and Inflammation. Genes 12, 552. https://doi.org/10.3390/genes12040552.

84. Rouhi, L., Auguste, G., Zhou, Q., Lombardi, R., Olcum, M., Pourebrahim, K., Cheedipudi, S.M., Asghar, S., Hong, K., Robertson, M.J., et al. (2022). Deletion of the Lmna gene in fibroblasts causes senescence-associated dilated cardiomyopathy by activating the double-stranded DNA damage response and induction of senescence-associated secretory phenotype. J. Cardiovasc. Aging 2, 30. https://doi.org/10.20517/jca.2022.14.

85. Liu, Y., Chen, X., Zhao, Y., Wang, X.-Y., Luo, Y.-W., Chen, L., Wang, W., Zhong, S., Hu, M., Dai, Z., et al. (2023). Small cytosolic double-stranded DNA represses cyclic GMP-AMP synthase activation and induces autophagy. Cell Rep. 42, 112852.

86. Nader, G.P.d.F., Agüera-Gonzalez, S., Routet, F., Gratia, M., Maurin, M., Cancila, V., Cadart, C., Palamidessi, A., Ramos, R.N., San Roman, M., et al. (2021). Compromised nuclear envelope integrity drives TREX1-dependent DNA damage and tumor cell invasion. Cell 184, 5230–5246.e22.

87. Verzi, M.P., McCulley, D.J., De Val, S., Dodou, E., and Black, B.L. (2005). The right ventricle, outflow tract, and ventricular septum comprise a restricted expression domain within the secondary/anterior heart field. Dev. Biol. 287, 134–145.

88. Lin, Z., von Gise, A., Zhou, P., Gu, F., Ma, Q., Jiang, J., Yau, A.L., Buck, J.N., Gouin, K.A., van Gorp, P.R.R., et al. (2014). Cardiac-specific YAP activation improves cardiac function and survival in an experimental murine MI model. Circ. Res. 115, 354–363.

89. Sancak, Y., Peterson, T.R., Shaul, Y.D., Lindquist, R.A., Thoreen, C.C., Bar-Peled, L., and Sabatini, D.M. (2008). The Rag GTPases bind raptor and mediate amino acid signaling to mTORC1. Science 320, 1496–1501.

90. Therneau, T.M., and Grambsch, P.M. (2013). Modeling Survival Data: Extending the Cox Model (Springer Science & Business Media).

91. Dobin, A., Davis, C.A., Schlesinger, F., Drenkow, J., Zaleski, C., Jha, S., Batut, P., Chaisson, M., and Gingeras, T.R. (2013). STAR: ultrafast universal RNA-seq aligner. Bioinformatics 29, 15–21.

92. Martin, B.K., Qiu, C., Nichols, E., Phung, M., Green-Gladden, R., Srivatsan, S., Blecher-Gonen, R., Beliveau, B.J., Trapnell, C., Cao, J., and Shendure, J. (2023). Optimized single-nucleus transcriptional profiling by combinatorial indexing. Nat. Protoc. 18, 188–207. https://doi.org/10.1038/s41596-022-00752-0.

93. Amezquita, R.A., Lun, A.T.L., Becht, E., Carey, V.J., Carpp, L.N., Geistlinger, L., Marini, F., Rue-Albrecht, K., Risso, D., Soneson, C., et al. (2020). Orchestrating single-cell analysis with Bioconductor. Nat. Methods 17, 137–145.

94. Germain, P.-L., Lun, A., Garcia Meixide, C., Macnair, W., and Robinson, M.D. (2021). Doublet identification in single-cell sequencing data using scDblFinder. F1000Res. 10, 979.

95. McCarthy, D.J., Campbell, K.R., Lun, A.T.L., and Wills, Q.F. (2017). Scater: pre-processing, quality control, normalization and visualization of single-cell RNA-seq data in R. Bioinformatics 33, 1179–1186.

96. Lun, A.T.L., McCarthy, D.J., and Marioni, J.C. (2016). A step-by-step workflow for low-level analysis of single-cell RNA-seq data with Bioconductor. F1000Res. 5, 2122.

97. Herzog, V.A., Reichholf, B., Neumann, T., Rescheneder, P., Bhat, P., Burkard, T.R., Wlotzka, W., von Haeseler, A., Zuber, J., and Ameres, S.L. (2017). Thiol-linked alkylation of RNA to assess expression dynamics. Nat. Methods *14*, 1198–1204.

98. Pham, T.V., Piersma, S.R., Warmoes, M., and Jimenez, C.R. (2010). On the beta-binomial model for analysis of spectral count data in label-free tandem mass spectrometry-based proteomics. Bioinformatics *26*, 363–369.

99. Wickham, H. (2016). ggplot2 (Springer New York).

100. Kim, Y., and Zheng, Y. (2013). Generation and characterization of a conditional deletion allele for Lmna in mice. Biochem. Biophys. Res. Commun. *440*, 8–13.

101. Sohal, D.S., Nghiem, M., Crackower, M.A., Witt, S.A., Kimball, T.R., Tymitz, K.M., Penninger, J.M., and Molkentin, J.D. (2001). Temporally regulated and tissue-specific gene manipulations in the adult and embryonic heart using a tamoxifen-inducible Cre protein. Circ. Res. *89*, 20–25.

102. Gay, L., Miller, M.R., Ventura, P.B., Devasthali, V., Vue, Z., Thompson, H.L., Temple, S., Zong, H., Cleary, M.D., Stankunas, K., and Doe, C.Q. (2013). Mouse TU tagging: a chemical/genetic intersectional method for purifying cell type-specific nascent RNA. Genes Dev. *27*, 98–115.

103. Chen, X., Zaro, J.L., and Shen, W.-C. (2013). Fusion protein linkers: property, design and functionality. Adv. Drug Deliv. Rev. *65*, 1357–1369.

104. Negrini, M., Wang, G., Heuer, A., Björklund, T., and Davidsson, M. (2020). AAV Production Everywhere: A Simple, Fast, and Reliable Protocol for In-house AAV Vector Production Based on Chloroform Extraction. Curr. Protoc. Neurosci. *93*, e103.

STAR★METHODS

KEY RESOURCES TABLE

REAGENT or RESOURCE	SOURCE	IDENTIFIER
Antibodies		
Anti-Lamin A/C	Abcam	Cat # Ab26300; RRID: AB_775965
Anti-Lamin A/C	Santa Cruz	Cat # sc-376248; RRID: AB_10991536
Anti-Lamin A/C	Santa Cruz	Cat # sc-20681; RRID:AB_648154
Anti-CD45 antibody	R&D Systems	Cat # AF114-SP; RRID: AB_442146
Anti-CD68 antibody	Cell Signaling	Cat # 97778; RRID: AB_2928056
Anti-γ-H2A.X antibody	Cell Signaling	Cat # 9718; RRID: AB_2118009
Anti-desmin antibody	Invitrogen	Cat # PA5-19063; RRID: AB_10977860
Anti-PCM-1 antibody	Sigma	Cat # HPA023370; RRID: AB_1855072
Anti-tdTomato antibody	OriGene	Cat # AB8181; RRID: AB_2722750
Anti-COX4 antibody	R&D Systems	Cat # MAB6980; RRID: AB_10973832
Anti-cGAS antibody	Cell Signaling	Cat # 31659; RRID: AB_2799008
Anti-STING antibody	Cell Signaling	Cat # 13647; RRID: AB_2732796
Anti-GAPDH antibody	ABclonal	Cat # AC001; RRID: AB_2619673
Alexa Fluor Plus 647 Phalloidin	ThermoFisher	Cat # A30107
Chemicals, peptides, and recombinant proteins		
Tamoxifen	Sigma	Cat #T5648
Collagenase Type II	Worthington	Cat # LS004177
Polyethylenimine, Linear, MW 25000, Transfection Grade (PEI 25K™)	Fisher Scientific	Cat # 23966-100
Target Retrieval Solution	DAKO	Cat #S2367
Corn oil	Sigma	Cat #C8267
Phenol/Chloroform/Isoamyl alcohol	Invitrogen	Cat # 15593031
Trizol LS	Invitrogen	Cat # 10296010
Heparin	Sagent Pharmaceuticals.	Cat # 25021-400-10
VectaStain ELITE ABC Kits	Vector Laboratories	Cat # PK-6100
DAB	DAKO	Cat #K3468
ProLong Glass Antifade Mountant	Invitrogen	Cat #P36984
Normal donkey serum	Jackson ImmunoResearch	Cat # 017-000-121
Sudan Black B	Electron Microscopy Slides	Cat # 21610
NEBuilder HiFi DNA Assembly Master Mix	NEB	Cat #E2621
Dulbecco's modified Eagle medium	Fisher Scientific	Cat # 11965-092
penicillin/streptomycin	Invitrogen	Cat # 105727
OptiPRO™-SFM	Thermo Fisher	Cat # 12309019
Fetal Bovine Serum	Sigma	Cat #F1051
Critical commercial assays		
Masson's Trichrome Kit	Thomas Scientific LLC	Cat # KTMTRPT
Click-iT™ Plus TUNEL Assay Kits for *In Situ* Apoptosis Detection; Alexa Fluor™ 488	Invitrogen	Cat #C10617
Luna Universal One-Step RT-qPCR Kit	New England Biolabs	Cat #E3005
NEBNext UltraII Directional RNA Library Prep Kit	New England Biolabs	Cat #E7760
Quant-seq 3′ mRNA-seq FWD kit	Lexogen	Cat #K01596
Deposited data		
RNA-seq raw and analyzed data	This paper	GEO: GSE241590

(Continued on next page)

Continued

REAGENT or RESOURCE	SOURCE	IDENTIFIER
Experimental models: Organisms/strains		
Lmna-LoxP mice	Jackson Laboratory	JAX stock No: 026284
Myh6-MerCreMer transgene mice	Jackson Laboratory	JAX stock No: 005657
Rosa26[CAG-LSL-tdTomato] mice	Jackson Laboratory	JAX stock No: 025106
Cgas-null mice	Jackson Laboratory	JAX stock No: 026554
CAG-Lox-Stop-Lox-Uprt transgene mice	Jackson Laboratory	JAX stock No: 021469
Sting-flox mice	Jackson Laboratory	JAX stock No: 031670
Mice carrying the *Mef2C-AHF-Cre* transgene allele	Verzi et al.[87]	https://doi.org/10.1016/j.ydbio.2005.08.041
Sting-null (generated from *Sting-LoxP* mouse)	This study	N/A
AAVpro 293T cell	TaKaRa	Cat # 632273
Oligonucleotides		
DNA oligonucleotide KI279 for *Lmna* genotype primer	Table_S3_oligonucleotides	Ikegami lab ID: KI279
DNA oligonucleotide KI280 for *Lmna* genotype primer	Table_S3_oligonucleotides	Ikegami lab ID: Ki280
DNA oligonucleotide EA062 for EGFP cloning	Table_S3_oligonucleotides	Ikegami lab ID: EA062
DNA oligonucleotide EA064 for EGFP with GS linker cloning	Table_S3_oligonucleotides	Ikegami lab ID: EA064
DNA oligonucleotide EA086 for icGAS (human cGAS with E225A/D227A amino acid substitutions)	Table_S3_oligonucleotides	Ikegami lab ID: EA086
DNA oligonucleotide EA087 for mouse cGAS	Table_S3_oligonucleotides	Ikegami lab ID: EA087
DNA oligonucleotide EA096 for *Cxcl10* qPCR primer	Table_S3_oligonucleotides	Ikegami lab ID: EA096
DNA oligonucleotide EA097 for *Cxcl10* qPCR primer	Table_S3_oligonucleotides	Ikegami lab ID: EA097
DNA oligonucleotide EA098 for *Ifnb1* qPCR primer	Table_S3_oligonucleotides	Ikegami lab ID: EA098
DNA oligonucleotide EA099 for *Ifnb1* qPCR primer	Table_S3_oligonucleotides	Ikegami lab ID: EA099
DNA oligonucleotide EA100 for *Ifit3* qPCR primer	Table_S3_oligonucleotides	Ikegami lab ID: EA100
DNA oligonucleotide EA101 for *Ifit3* qPCR primer	Table_S3_oligonucleotides	Ikegami lab ID: EA101
DNA oligonucleotide KI444 for *Actb* qPCR primer	Table_S3_oligonucleotides	Ikegami lab ID: KI444
DNA oligonucleotide KI445 for *Actb* qPCR primer	Table_S3_oligonucleotides	Ikegami lab ID: KI445
DNA oligonucleotide KI466 for AAV titering primer	Table_S3_oligonucleotides	Ikegami lab ID: KI466
DNA oligonucleotide KI467 for AAV titering primer	Table_S3_oligonucleotides	Ikegami lab ID: KI467
Recombinant DNA		
pAAV:cTNT::Luciferase	Lin et al.[88]	pAAV:cTNT::Luciferase; Addgene plasmid #69915
pAAV:cTNT::GFP-GS linker	This paper	Ikegami lab ID: bAE263_1
pAAV:cTNT::GFP-icGAS	This paper	Ikegami lab ID: bAE299_1
pAAV:cTNT:cGAS	This paper	Ikegami lab ID: bAE299_3
pLJM1-EGFP	Sancak et al.[89]	pLJM1-EGFP; Addgene plasmid #19319
Software and algorithms		
ImageJ	N/A	https://imagej.net/ij/
NIS Elements	Nikon Instruments Inc.	RRID:SCR_014329
Odyssey CLx Imaging System	LI-COR Biosciences	https://www.licor.com/bio/odyssey-dlx/
CellProfiler	Broad Institute	https://cellprofiler.org/
R	R Core Team	https://www.R-project.org/
survival package	Therneau and Grambsch[90]	https://cran.r-project.org/web/packages/survival/index.html
survminer package	N/A	https://cran.r-project.org/web/packages/survminer/index.html
STAR version 2.7.9	Dobin et al.[91]	https://github.com/alexdobin/STAR

Continued

REAGENT or RESOURCE	SOURCE	IDENTIFIER
DESeq2	Love et al.[55]	https://bioconductor.org/packages/release/bioc/html/DESeq2.html
Metascape	Zhou et al.[54]	https://metascape.org/gp/index.html
sci-RNA-seq3 pipeline	Martin et al.[92]	https://github.com/JunyueC/sci-RNA-seq3_pipeline
sci-RNA-seq analysis workflow	This paper	https://github.com/kohta-ikegami/En_CellReports_2024/
SingleCellExperiment package	Amezquita et al.[93]	https://www.bioconductor.org/packages/release/bioc/html/SingleCellExperiment.html
scDblFinder package	Germain et al.[94]	https://bioconductor.org/packages/release/bioc/html/scDblFinder.html
scuttle package	McCarthy et al.[95]	https://www.bioconductor.org/packages/release/bioc/html/scuttle.html
scran package	Lun et al.[96]	https://bioconductor.org/packages/release/bioc/html/scran.html
scater package	McCarthy et al.[95]	https://bioconductor.org/packages/release/bioc/html/scater.html
R packages *GO.db*	N/A	https://bioconductor.org/packages/release/data/annotation/html/GO.db.html
KEGGREST	N/A	https://bioconductor.org/packages/release/bioc/html/KEGGREST.html
CellChat package	Jin et al.[77]	https://github.com/sqjin/CellChat
slamdunk package	Herzog et al.[97]	https://github.com/t-neumann/slamdunk
countdata package	Pham et al.[98]	https://www.rdocumentation.org/packages/countdata/versions/1.3
ggplot2 package	Wickham[99]	https://ggplot2.tidyverse.org/
Other		
Bio-Rad CFX96 Real-Time PCR Detection System	Bio-Rad	RRID:SCR_018064
Yokogawa CSU-W1 Sora spinning disk confocal microscope	Nikon Instruments Inc.	https://www.microscope.healthcare.nikon.com/products/confocal-microscopes/csu-series/csu-w1
Nikon A1R laser-scanning confocal microscope	Nikon Instruments Inc.	RRID:SCR_020317
Automated Genotyping Services	Transnetyx, Inc.	https://www.transnetyx.com/
Gencode M27 Basic gene annotation	The National Human Genome Research Institute	https://www.gencodegenes.org/mouse/release_M27.html

RESOURCE AVAILABILITY

Lead contact
Further information and requests for resources and reagents should be directed to and will be fulfilled by the lead contact, Kohta Ikegami (Kohta.Ikegami@cchmc.org).

Materials availability
All mice are available at the sources specified in Key resources table. Plasmids produced in this study are provided upon request from the lead contact after material transfer agreements. Any information required to reanalyze the data reported in this paper is available from the lead contact.

Data and code availability
- High-throughput sequencing data have been deposited at Gene Expression Omnibus (http://www.ncbi.nlm.nih.gov/geo/) and are publicly available as of the date of publication. Accession numbers are listed in Key resources table.
- This paper does not report original codes.
- Any additional information required to reanalyze the data reported in this paper is available from Lead Contact upon request.

EXPERIMENTAL MODEL AND STUDY PARTICIPANT DETAILS

Mouse genetics and treatment

Lmna-LoxP mice[100] were provided by Dr. Yixian Zheng at Carnegie Institution and are available at the Jackson Laboratory (JAX stock no: 026284). *Myh6-MerCreMer* (Myh6MCM) mice[101] (JAX stock No: 005657), *Rosa26$^{CAG-LSL-tdTomato}$* ("Ai75") mice[58] (JAX stock No: 25106), *Cgas-null* mice[67] (JAX stock No: 026554), and *CAG-Lox-Stop-Lox-Uprt* mice[102] (*Uprt^{Tg}*; JAX stock No: 021469) were obtained from the Jackson Laboratory. *Sting-null* mice were generated by breeding *Sting-flox* mice,[68] obtained from the Jackson Laboratory (JAX stock No: 031670), with Cre deleter mice (*Mef2C-AHF-Cre* mice[87]) provided by Dr. Brian L. Black at the University of California San Francisco. For cardiomyocyte-specific *Lmna* knockout experiments, *Lmna$^{F/F}$;Myh6MCM$^{Tg/0}$* (*Lmna^{CKO}*) and *Lmna$^{+/+}$;-Myh6MCM$^{Tg/0}$* (wild-type control) mice were used. For the analysis of nuclear tdTomato intensity, *Lmna$^{F/F}$;Myh6MCM$^{Tg/0}$;Rosa26-$^{CAG-LSL-tdTomato/+}$* and *Lmna$^{+/+}$;Myh6MCM$^{Tg/0}$;Rosa26$^{CAG-LSL-tdTomato/+}$* mice were used. For SLAM-IT-seq experiments, *Lmna$^{F/F}$;Myh6MCM$^{Tg/0}$;Uprt$^{Tg/0}$*, *Lmna$^{+/+}$;Myh6MCM$^{Tg/0}$;Uprt$^{Tg/0}$*, *Lmna$^{F/F}$;Myh6MCM$^{Tg/0}$;Uprt$^{0/0}$*, and *Lmna$^{+/+}$;Myh6MCM$^{Tg/0}$;Uprt$^{0/0}$* mice were used. For *Cgas* deletion experiments, *Cgas$^{-/-}$;Lmna$^{F/F}$;Myh6MCM$^{Tg/0}$* mice, *Cgas$^{+/+}$;Lmna$^{F/F}$;Myh6MCM$^{Tg/0}$*, *Cgas$^{+/+}$;Lmna$^{F/+}$;Myh6MCM$^{Tg/0}$*, and *Cgas$^{-/-}$;Lmna$^{F/+}$;Myh6MCM$^{Tg/0}$* mice were used. For *Sting* deletion experiments, *Sting$^{-/-}$;Lmna$^{F/F}$;Myh6MCM$^{Tg/Tg}$* mice, *Sting$^{+/+}$;Lmna$^{F/F}$;Myh6MCM$^{Tg/Tg}$*, *Sting$^{+/+}$;Lmna$^{F/+}$;Myh6MCM$^{Tg/Tg}$*, and *Sting$^{-/-}$; Lmna$^{F/+}$;Myh6MCM$^{Tg/Tg}$* mice were used. All mice used in experiments were administered with tamoxifen (Sigma, T5648) at 6–8 weeks of age via intraperitoneal injections (100 μL of 4 mg/mL solution per day for 4 consecutive days) dissolved in corn oil (Sigma, C8267). All mice were used in mixed genetic backgrounds and both sexes. All mouse experiments were approved by the Institutional Animal Care and Use Committee (IACUC) at Cincinnati Children's Hospital under IACUC protocol 2021-0014 or at University of Chicago under IACUC protocol 71730-10. All procedures were performed in compliance with institutional and governmental regulations under PHS Animal Welfare Assurance number D16-00068 (Cincinnati Children's) or D16-00322 (University of Chicago).

METHOD DETAILS

Mouse genotyping

For genotyping of the *Lmna* alleles, genomic DNA of isolated cardiomyocytes was extracted with Phenol/Chloroform/Isoamyl alcohol (Invitrogen,15593-031), treated with RNaseA and Proteinase K, and purified. Floxed, recombined, and wild type *Lmna* alleles were detected by PCR using the primers KI279 and KI280 (Table S3). Based on the agarose gel (1.5%) analysis of PCR-amplified products, recombination efficiency (%) was calculated by 153-bp band (Recombined) over 598-bp band (Floxed) intensities. Genotyping of *Myh6-MerCreMer*, *Cgas*, *Sting*, *Uprt*, and *Rosa26::CAG-LSL-tdTomato* alleles was performed at Transnetyx, Inc.

Echocardiography

The transthoracic echocardiography was performed using a Vevo 3100 LT (FUJI FILM VisualSonics) and a transducer of 50-MHz MX-700. Parasternal long-axis view and short-axis view at the papillary muscle level were imaged. Two-dimensional M-mode tracing was recorded at three or more consecutive cardiac cycles. Data were analyzed using Vevo LAB Software Package V3.2.6. Echocardiographic parameters between two groups were compared using Wilcoxon rank sum tests, and *p*-values were adjusted for multiple testing using the Benjamini-Hochberg procedure in R.

Survival analysis

Kaplan-Meier survival analyses were performed using the *survival* package[90] and visualized using the *survminer* package in R (Key resources table). Log rank tests were performed using the *survdiff* function in the *survival* package.

Histological staining

Hearts were perfused with 100 mM KCl and fixed in 10% Formalin (Fisherbrand, 245–685). Fixed hearts were embedded in paraffin and sectioned to a thickness of 5 μm. Heart sections were stained with hematoxylin and eosin (H&E) or a Masson's Trichrome Kit (Thomas Scientific LLC, KTMTRPT) according to the manufacturer's protocol.

Cardiomyocyte isolation

Mice were administered with heparin (100 Units, NDC 25021-400-10), anesthetized with Isoflurane, and euthanized by cervical dislocation. Hearts were perfused with 100 mM KCl and moved to Tyrode's solution (10 mM glucose, 5 mM HEPES, 5.4 mM KCl, 1.2 mM MgCl$_2$, 150 mM NaCl and 2 mM sodium pyruvate, pH 7.35). Excised hearts were cannulated to the Langendorff retrograde perfusion system through the aorta and perfused with Base solution (Tyrode's solution with 10 mM taurine and 12 mM 2,3-butanedione monoxime) and then digested with prewarmed Digestion buffer (Base solution with 180 U/mL Collagenase Type II (Worthington, LS004177) and 25 μM CaCl$_2$) for 20 min at 37°C. Heart tissue was then isolated, gently minced in Base solution containing 5 mg/mL BSA. Cell suspension was filtrated through a 240 μm mesh. Cardiomyocytes settled to the bottom of conical tubes by gravity were used in experiments.

Immunohistochemistry

Deparaffinized heart tissue sections, that had been fixed with 10% formalin, were subjected to heat-induced antigen retrieval in Target Retrieval Solution (S2367, DAKO) for 5 min. Antigen-retrieved sections were incubated with anti-Lamin A/C antibody Ab26300 (rabbit, Abcam) (1:400) for 1 h at room temperature, followed by biotinylated anti-rabbit IgG antibody for 30 min at room temperature. The antigen-antibody binding was detected by Elite kit (PK-6100, Vector Laboratories) and DAB (DAKO, K3468) system. Sections were counterstained by hematoxylin.

Immunofluorescence on tissue sections

Deparaffinized heart tissue sections, that had been fixed with 10% formalin, were subjected to heat-induced antigen retrieval in 10 mM Tris EDTA buffer (pH 9.0) for 5 min. Antigen-retrieved sections were incubated overnight at 4°C with goat anti-CD45 antibody (R&D Systems, AF114-SP) and rabbit anti-CD68 antibody (Cell Signaling, 97778), or rabbit anti-γ-H2A.X antibody (Cell Signaling, 9718) and goat anti-desmin antibody (Invitrogen, PA5-19063), or rabbit anti-PCM1 antibody (Sigma, HPA023370), goat anti-TdTomato antibody (OriGene, AB8181), and mouse anti-Cox4 antibody (R&D Systems, MAB6980), followed by Alexa fluorophore-conjugated secondary antibodies for 1 h at 37°C. Cells were counterstained with DAPI (4′,6-diamidino-2-phenylindole), submerged in 0.25% Sudan Black B (Electron Microscopy Slides, #21610) in 70% Isopropanol for 10 min, and then mounted with ProLong Glass Antifade Mountant (Invitrogen, P36984). Fluorescence signals and imaging were acquired using a Nikon A1R laser-scanning confocal microscope. CD45 and CD68 quantification of whole heart tissue was performed using Nikon NIS-Elements; each genotype had five biological replicates. CD45/CD68 positive cells were identified based on the overlap of the DAPI signal with CD45/CD68. Signal intensities between two groups were compared using Wilcoxon rank sum tests in R. For γ-H2A.X quantification, nuclei with DAPI were counted and those with at least one γ-H2A.X focus were quantified using CellProfiler. Five to eight images per mouse (374 × 374 μm^2 per image) were used for the quantification.

Immunofluorescence on isolated cardiomyocytes

Isolated cardiomyocytes were fixed in 4% paraformaldehyde (Electron Microscopy Slides, #15710) in PHEM buffer (60 mM PIPES pH7.5, 25 mM HEPES pH7.5, 10 mM EGTA, 4 mM MgSO$_4$) for 10 min at 37°C, then washed with PBS and attached to coverslips with Cell-Tak Cell Adhesive (Sigma Aldrich, 354240). Cells were blocked and permeabilized in a buffer containing 5% normal donkey serum (Jackson ImmunoResearch, 017-000-121), 1% non-fat milk, and 0.1% Triton X-100 in PBS for 1 h at 37°C. Permeabilized cells were incubated overnight at 4°C with mouse anti-Lamin A/C antibody (Santa Cruz, sc-376248), rabbit anti-PCM-1 antibody (Sigma, HPA023370), mouse anti-cGAS antibody (Cell Signaling, D3O8O). Cells were washed and incubated with Alexa fluorophore-conjugated secondary antibodies and Alexa Fluor Plus 647 Phalloidin for 1 h at 37°C. Cells were counterstained with DAPI and then mounted with ProLong Glass Antifade Mountant. Fluorescence signals were detected on Nikon A1R laser-scanning confocal microscope or Yokogawa CSU-W1 Sora spinning disk confocal microscope.

Plasmid construction

The expression vectors used in this study were derived from the pAAV:cTNT::Luciferase vector (gift from William Pu; Addgene plasmid # 69915).[88] For cloning of pAAV:cTnT:cGAS and pAAV:cTnT::GFP vectors, we digested the pAAV:cTNT::Luciferase vector with *NheI* and *NotI*, and the luciferase gene was replaced with the cGAS or EGFP sequences using NEBuilder HiFi DNA Assembly Master Mix (NEB E2621). The pAAV:cTnT::GFP-icGAS vector was generated by inserting the catalytically-inactive cGAS (icGAS) sequence (Oligonucleotide ID: EA086, Table S3) into the pAAV:cTnT::GFP vector digested with *NotI*. The icGAS sequence was derived from the human cGAS protein sequence with an E225A/D227A amino acid substitution that abolishes enzyme activity and interferon production, but retains DNA binding ability and functions, used as an NE rupture marker previously.[60] The DNA fragments for mouse wild-type *Cgas* (NM_173386.5) and *icGAS* were synthesized using gBlocks Gene Fragment synthesis service (Integrated DNA Technologies). *EGFP* with a flexible GS linker (GGGGS) at the C terminus[103] was amplified from the pLJM1-EGFP vector (gift from David Sabatini; Addgene plasmid #19319)[89] using the EA062 and EA064 primers (Table S3).

MyoAAV production and *in vivo* transduction

For myoAAV production, we used a published protocol with modifications.[104] We co-transfected the pAAV-cTnT-transgene vector (see above), the pHelper vector (GenBank: AF369965.1), and the pRep/Cap 1A-MYO capsid vector[59] into AAVpro 293T cells (TaKaRa, 632273) using polyethylenimine (PEI) reagent. The 1A-MYO capsid vector allows production of muscle-tropic AAV9 derivative (MyoAAV).[59] The transfected cells were cultured in the OptiPRO-SFM medium (Thermo Fisher, 12309019) for 72 h at 37°C to produce the virus. Cells and the culture media were collected for AAV purification. AAV particles were extracted with chloroform, precipitated with polyethylene glycol, purified with DNase/RNase digestion followed by chloroform extraction, and concentrated in PBS with Amicon filters (Millipore), as detailed in a previous report.[104] The viral genome copy numbers (vg) were estimated by qPCR using primers amplifying the cTnT promoter region (Oligonucleotide ID KI466 and KI467, Table S3). MyoAAV particles were administered to mice through retro-orbital venous sinus injection at a dose of 2×10^{11} vg per mouse at 4 weeks of age, which was 14–15 days prior to tamoxifen.

Image quantification related to nuclear envelope ruptures

For quantification of nuclei with PCM1-lost nuclear tips and DNA protrusion, we used immunofluorescent images of isolated cardiomyocytes stained for PCM1 and counter-stained with DAPI (DNA) and Phalloidin (F-actin). Rod-shaped cardiomyocytes that had a well-defined sarcomere structure based on Phalloidin staining and two or more nuclei were used for quantification. We quantified instances of DAPI signal protrusion from a nuclear envelope site at which PCM1 signals were specifically discontinued ("local PCM1 loss"). The percentage of cells with one or more nuclei with a local PCM1 loss and the number of such nuclei per cell were quantified manually post imaging. We obtained the percentage from >50 cardiomyocytes per animal with a total of 3 animals per genotype. The percentages of cardiomyocytes with PCM1-lost nuclei were compared between genotypes using unpaired one-tailed Welch's t-tests in R.

For quantification of nuclei with icGAS puncta, we used isolated cardiomyocytes from wild-type or $Lmna^{CKO}$ mice treated with MyoAAV-GFP-icGAS. The percentage of cells with icGAS puncta was quantified manually post imaging. We obtained the percentage from >50 cardiomyocytes per animal with a total of 3 animals per genotype. The icGAS-positive cardiomyocyte percentages were compared between genotypes using an unpaired one-tailed Welch's t test in R.

For quantification of NLS-tdTomato intensities, we used $Lmna^{F/F};Myh6MCM^{Tg/0};Rosa26^{CAG-LSL-tdTomato/+}$ and $Lmna^{+/+};Myh6MCM^{Tg/0};Rosa26^{CAG-LSL-tdTomato/+}$ mice. Isolated cardiomyocytes were fixed, immunostained for PCM1, and counterstained with DAPI. Quantification of NLS-tdTomato signals was performed in the Fiji image analysis software. Cardiomyocytes that had two or more nuclei were used for quantification. Nuclei with nuclear envelope ruptures were identified as described above. A freehand-drawn area was placed inside a nucleus for quantification of the nuclear tdTomato signal. A nucleus was selected for quantification using the following algorithm: If a cell had only ruptured nuclei, one ruptured nucleus was randomly selected for quantification; if a cell had both ruptured and unruptured nuclei, one ruptured nucleus was randomly selected for quantification; if a cell had only unruptured nuclei, one unruptured nucleus was randomly selected for quantification. For each nucleus, whether it had a local PCM1 loss with DNA protrusion was manually determined as described above. A second quantification area of the same size as the nuclear area was placed in the cytoplasm for cytoplasmic tdTomato signal quantification. For each of the two areas, a mean NLS-tdTomato pixel intensity was measured using the ROI manager function in Fiji. We performed this quantification process for three mice per genotype. In total, we had quantification information for 99 wild-type cardiomyocytes (all intact PCM1), 90 $Lmna^{CKO}$ cardiomyocytes with local PCM1 loss, and 36 $Lmna^{CKO}$ cardiomyocytes with intact PCM1. Signal intensities between two groups were compared using Wilcoxon rank sum tests, and p-values were adjusted for multiple testing using the Benjamini-Hochberg procedure in R.

TUNEL assay

TUNEL assays were performed on deparaffinized heart sections using a Click-iT Plus TUNEL Assay kit for *In Situ* Apoptosis Detection (Invitrogen, C10617), according to the manufacturer's instruction. The samples were then co-stained with Alexa Fluor Plus 647 Phalloidin (Invitrogen, A30107) for 1 h at 37°C to visualize cells in tissue sections. For positive controls, sample tissues were treated with DNase I prior to the TUNEL assay. The number of cells with positive staining in the TUNEL assay (TUNEL$^+$ cells) was determined using sections from three hearts per genotype. TUNEL positive cells in 2–3 images per mouse (257×257 μm^2 per image) were counted manually and compared between two groups using Wilcoxon rank sum tests in R.

Immunoblot

Snap-frozen hearts or isolated cardiomyocytes were lysed in the RIPA buffer for cGAS and STING immunoblotting (20 mM Tris-HCl, 150 mM NaCl, 1% IGEPAL, 0.5% sodium deoxycholate, 0.1% SDS, 10 mM dithiothreitol, protease and phosphatase inhibitors) or the Urea buffer for Lamin A/C immunoblotting (20 mM HEPES pH 7.4, 1 M NaCl, 8 M urea, protease and phosphatase inhibitors). Proteins were extracted using pestle homogenization and sonication. Cell lysates were centrifuged at 13,000 rpm for 5 min at 4°C, and proteins in the supernatant were separated by SDS-PAGE. Proteins were transferred to a PVDF membrane. Membranes were blocked with nonfat milk. The primary antibodies were rabbit anti-Lamin A/C antibody (Santa Cruz, sc-20681, 1:1000), rabbit anti-cGAS antibody (Cell Signaling, #31659, 1:500), rabbit anti-STING antibody (Cell Signaling, #13647, 1:500), and rabbit anti-GAPDH antibody (ABclonal, AC001, 1:1000); Secondary antibodies were anti-rabbit or anti-mouse IgG (H + L) DyLight 680 and 800 (Cell Signaling, 1:5000). Signals were detected and quantified in the Odyssey CLx Imager (LI-COR). Gels after protein transfer were counter-stained with Coomassie to evaluate the loaded protein amount.

Electron microscopy

Heart tissues were dissected and fixed in 2.5% glutaraldehyde, post-fixed in 1% OsO4 for 1 h at 4°C, rinsed, dehydrated in ethanol, and infiltrated overnight. The semithin Epon sections were screened by light microscopy to select areas with the longitudinal orientation of myocytes that were subsequently processed to prepare thin sections. The sections were stained with 1% uranyl acetate, followed by lead citrate. The sections were imaged using Hitachi Model H-7650 Transmission Electron Microscope at Cincinnati Children's Integrated Pathology Research Facility.

Quantitative reverse-transcriptase PCR (RT-PCR)

For RT-PCR analysis, we used wild-type treated with MyoAAV-Luciferase ($n = 5$) or MyoAAV-cGAS ($n = 3$) and $Lmna^{CKO}$ mice treated with MyoAAV-Luciferase ($n = 4$) or MyoAAV-cGAS ($n = 5$) at 2 weeks post tamoxifen. Total RNAs of isolated cardiomyocytes were

extracted with Trizol LS (Invitrogen, 10296010), treated with DNaseI, and purified. Quantitative RT-PCR was conducted with the Luna Universal One-Step RT-qPCR Kit (NEB, E3005) on a Bio-Rad CFX96 Real-Time PCR Detection System (Bio-Rad) following the manufacturer's instructions. The primers for mouse genes were: EA096 and EA097 for *Cxcl10*; EA098 and EA099 for *Ifnb1*; EA100 and EA101 for *Ifit3*; and KI444 and KI445 for *Actb* (Table S3). The delta-delta Ct method was used to quantify mRNA abundance with *Actb* as a normalization control. mRNA levels between two groups were compared using Wilcoxon rank sum tests, and *p*-values were adjusted for multiple testing using the Benjamini-Hochberg procedure in R.

RNA-seq
For RNA-seq comparing wild-type mice with *Lmna^CKO* mice at different post tamoxifen times, we used wild-type (*n* = 5) and *Lmna^CKO* mice (*n* = 4) at 1 week post tamoxifen, wild-type (*n* = 3) and *Lmna^CKO* mice (*n* = 2) at 11 days post tamoxifen, and wild-type (*n* = 7) and *Lmna^CKO* mice (*n* = 5) at 2 weeks post tamoxifen. For RNA-seq analysis of *Lmna/Cgas* double knockout mice, we used *Cgas*^{−/−}; *Lmna^F/F;Myh6MCM* mice (*n* = 4), *Cgas*^{+/+};*Lmna^F/F;Myh6MCM* (*n* = 6), *Cgas*^{+/+};*Lmna^F/+;Myh6MCM* (*n* = 6), and *Cgas*^{−/−};*Lmna^F/+;Myh6MCM* (*n* = 4) for experiments. Hearts were perfused with 100 mM KCl and removed for RNA extraction. Total RNAs were extracted with Trizol LS (Invitrogen, 10296010), treated with DNaseI, and purified. For tamoxifen time course experiments, mRNA sequencing libraries were generated using the poly-A selection module in the NEBNext UltraII Directional RNA Library Prep Kit (NEB E7760) and sequenced on the Illumina HiSeq 2500 sequencer with single-end 50 cycles. For *cGas/Lmna* double knockout experiments, libraries were generated using QuantSeq 3′ mRNA-Seq Library Prep Kit FWD (Lexogen, K01596) and sequenced on the Illumina NovaSeq 6000 sequencer with single-end 100 cycles.

RNA-seq analysis
High-throughput sequencing reads were aligned to the mouse mm39 reference genome with the Gencode vM27 basic gene annotation using STAR version 2.7.9 [91] with the default alignment parameters except using "clip3pAdapterSeq AGATCGGAA GAGCACACGTCTGAACTCCAGTCA". From raw read counts per transcript, TPMs (transcripts per million) were calculated in R as follows: $TPM = 10^6 \times RPK/sum(RPK)$, where RPK = read count/transcript length in kp, and sum(RPK) is the sum of RPKs for all transcripts. Raw read counts were used for differential gene expression analyses using DESeq2 [55] in R. Protein-coding or lncRNA genes with adjusted *p*-value <0.05 and absolute $\log_2$ fold change >1 (NEB Directional RNA-seq) or with adjusted *p*-value <0.05 and absolute $\log_2$ fold change >0 (QuantSeq 3′ mRNA-seq) were considered differentially expressed genes (Table S1). Differentially expressed genes were analyzed for the enrichment of GO Biological Processes, GO Molecular Functions, GO Cellular Components, and KEGG pathway terms using Metascape [54] with the default enrichment parameters.

Single-nucleus RNA-seq
For single-nucleus RNA-seq, we used wild-type (*n* = 3) and *Lmna^CKO* mice (*n* = 3) at 2 weeks post tamoxifen. Combinatorial indexing-based single-nucleus RNA-seq was conducted according to the optimized sci-RNA-seq3 protocol developed previously.[92] Briefly, mice were anesthetized with isoflurane, euthanized by cervical dislocation, and then hearts were perfused with 100 mM KCl. Removed hearts were diced into small pieces in cold PBS containing Diethyl pyrocarbonate (DEPC, Sigma D5758). Fresh heart pieces were dounce-homogenized to liberate nuclei in Hypotonic lysis buffer B (7.7 mM Na_2HPO_4, 4.5 mM NaH_2PO_4, 1.8 mM KH_2PO_4, 2.7 mM KCl, 10.3 mM NaCl, 3 mM $MgCl_2$, 0.08% BSA, 0.025% Igepal CA-630, 1% DEPC) and passed through cell strainers. Nuclei were fixed in 1 mg/mL dithiobis(succinimidyl propionate) (DSP, Thermo Fisher 22585) for 15 min on ice, washed, and stored at −80°C until use. For each mouse, 50,000 nuclei were placed in each of 8 wells of a 96-well plate (a total 48 wells for 6 mice). The remaining 48 wells were filled with similarly processed mouse heart nuclei with comparable sample quality from an unrelated project. Nuclei were subjected to reverse transcription with 96-indexed poly-T RT primers that contained a unique molecular identifier (UMI) sequence (3lvl_mRNA_RT_plate_1; Table S3). Nuclei from all wells were combined and redistributed evenly to 96 wells. Redistributed cells were subjected to ligation with 96-indexed ligation primers in 96 wells (3lvl_mRNA_Lig_plate_1; Table S3). Nuclei from all wells were combined again and redistributed evenly to 96 wells at 1,000 nuclei per well. Redistributed cells underwent second strand synthesis, protease digestion, tagmentation using N7-loaded Tn5 transposase (Oligonucleotide ID KI455 and KI456, Table S3), and PCR-amplified using 96-indexed PCR P7 primers (PCR_P7_plate1; Table S3) and the unindexed P5 primer (Oligonucleotide ID KI454, Table S3), for 16 cycles. PCR amplicons were combined and size-selected for DNA fragments between 250 bp and 600 bp. Purified library DNA were sequenced for 50 bases on the paired-end mode (34 cycles on Read1 to sequence the ligation index, UMI, and the RT barcode; 10 cycles on Index1 to sequence the P7 index; and 48 cycles on Read2 to sequence the cDNA) using an Illumina NovaSeq6000 sequencer.

Single-nucleus RNA-seq analysis
Pre-processing of the single-nucleus RNA-seq data was performed using the published sci-RNA-seq3 pipeline.[92] The sci-RNA-seq3 pipeline takes fastq files separated by the P7 index as input, aligns reads to the genome, and returns a gene-by-cell read count matrix. First, raw reads were trimmed to remove poly A tails, aligned to the mm39 mouse reference genome using STAR,[91] and filtered for MAPQ greater than or equal to 30. Duplicate reads were removed based on UMI. Read counts per gene were computed for each cell defined by the unique combination of the RT index, ligation index, and P7 index. The gene-by-cell count matrix produced by the sci-RNA-seq3 pipeline was further processed in the *SingleCellExperiment* package framework in R.[93] We used the *scDblFinder*

package[94] for doublet detection and the *scuttle* package[95] for mitochondrial RNA quantification in R. We obtained 14,111 nuclei after filtering for nuclei with the *scDblFinder* doublet score less than 0.25 and mitochondrial RNA contamination percentage less than 2% of total RNAs per cell. Read counts for a gene were normalized by per-cell read depth and then log-transformed to obtain normalized expression values ("logcounts"). Logcounts were used to plot expression values in graphs. Principal component analysis (PCA) was performed on logcounts for top 2,000 highly variable genes across cells using the *fixedPCA* function in the *scran* package.[96] The top 50 principal components were used in the *runUMAP* function in the *scater* package[95] with n_neighbors = 20 and min_dist = 1 parameters to obtain UMAP dimensions. To cluster cells, logcounts were processed in the *clusterCells* function in the *scran* package using the top 50 principal components, with the number of nearest neighbors k = 12. Cell clusters were annotated manually with cell type names based on marker gene expression. Per-gene read counts were summed within cell groups and processed by the *DESeq2* package[55] to perform pseudo-bulk differential gene expression analysis. Genes with adjusted *p*-values smaller than 0.05 were defined as differentially expressed genes (Table S4). GO analysis of differentially expressed genes was performed as described in the RNA-seq analysis section using Metascape.[54] For the analysis of the enrichment within selected GO and KEGG terms, all genes associated with the selected terms were obtained using the R packages *GO.db* and *KEGGREST*, and enrichment of differentially expressed genes among these genes was computed by Fisher's exact test with *p*-values adjusted by the Benjamini-Hochberg procedure. Cell-cell communication analysis was performed using the *CellChat* package in R[77] using the 12 cell type annotations and the default mouse database with a minimum of ten cells for the analysis. Positive communications were selected by the *subsetCommunication* function in *CellChat* with threshold *p*-value less than 0.05, and the reported interaction counts were used to plot data. All software and packages used in the analysis are listed in Key resources table.

SLAM-IT-seq

For SLAM-IT-seq experiments, we used $Lmna^{F/F};Myh6MCM^{Tg/0};Uprt^{Tg/0}$ (n = 6) and $Lmna^{+/+};Myh6MCM^{Tg/0};Uprt^{Tg/0}$ (n = 8) mice as experimental groups, and $Lmna^{F/F};Myh6MCM^{Tg/0};Uprt^{0/0}$ (n = 4) and $Lmna^{+/+};Myh6MCM^{Tg/0};Uprt^{0/0}$ (n = 3) mice as negative control groups that would not incorporate 4-thiouracil (4sU) due to the absence of the *Uprt* allele. All mice were administered with tamoxifen and used at 2 weeks post tamoxifen treatment. SLAM-IT-seq was conducted according to a previously established protocol.[62] Briefly, mice were intraperitoneally injected with 4-thiouracil (4sU) dissolved in a DMSO/corn oil (1:3) solution at a dose of 10 mg per gram of body weight. Six hours after the injection, mice were sacrificed, and hearts were perfused with 100 mM KCl and removed. RNAs from the left ventricular free wall were extracted by Trizol LS, purified, and DNaseI-treated using Directzol RNA miniprep kit (Zymo, R2052). Purified RNAs (1.5 μg) were subjected to alkylation in the presence of 12 mM Iodoacetamide (IAA, Sigma I1149). High-throughput sequencing libraries were generated from the alkylated RNAs using Quant-seq 3′ mRNA-seq FWD kit (Lexogen K01596) and sequenced 100 bases on the single-end mode on an Illumina NovaSeq6000 sequencer.

SLAM-IT-seq analysis

We analyzed SLAM-IT-seq data according to the published SLAM-IT-seq data analysis pipeline that uses the *slamdunk* package[97] and R functions.[62] First, raw reads were processed by the *slamdunk all* function in the the *slamdunk* package with the following alignment parameters: –trim-5p 12 –topn 100 –multimap –max-read-length 101 with default –var-fraction (0.8) and default -c (1). This function aligned reads to 3′ UTRs of Gencode vM27 genes (total 208,307 UTRs from 37,065 unique genes) in the mm39 mouse reference genome. Aligned reads were processed by the *alleyoop utrrates* function in the *slamdunk* package with default parameters to quantify C-to-T conversion events. UTRs with at least one read coverage for all 21 samples were retained for further analyses (47,717 UTRs from 14,250 unique genes). Statistically significant C-to-T conversion events in each transcript (i.e., the likelihood of cardiomyocyte-derived transcripts) were identified by comparing the conversion events in mice carrying the *Uprt* allele with those in mice not carrying this allele using beta-binomial test with the *bbtest* function[98] in the *countdata* package in R. P-values of the beta binomial test were adjusted with the Benjamini-Hochberg procedure for multiple tests (Table S2). A transcript with the lowest adjusted *p*-value was chosen to represent a gene if there were multiple transcripts per gene. Genes with adjusted *p*-values smaller than 0.05 were defined as originating from cardiomyocytes, whereas genes with adjusted *p*-values greater than or equal to 0.05 were defined as not originating from cardiomyocytes. All software and packages used in the analysis are listed in Key resources table.

QUANTIFICATION AND STATISTICAL ANALYSIS

Statistical tests were performed using the following procedures: Wilcoxon tests with a Benjamini-Hochberg-adjusted *p*-value threshold of 0.05 computed by base R functions (Figures 1E, 2F, 2K, 2L, 3E, 3H, S1D, and S1E); Log rank tests with a *p*-value threshold of 0.05 computed by the *survival* package in R[90] (Figures 1F, 3J, and S3I); Generalized linear model with a Benjamini-Hochberg-adjusted *p*-value threshold of 0.05 computed by the DESeq2 package in R[55] (Figures1G, 1I, 3G, 4C, 4E, 4F, S3G, and S4E); Metascape[54] (Figures 1H, 3B, 4D, S3F, S4C, and S4F); unpaired one-tailed Welch's t test with a *p*-value threshold of 0.05 computed by base R functions (Figures 2I and 2J); Beta binomial test with a Benjamini-Hochberg-adjusted *p*-value threshold of 0.05 computed by base R functions (Figures S3D and S3E); and Fisher's exact test with Benjamini-Hochberg-adjusted *p*-value threshold of 0.05 (Figure S4D).

Statistical details of experiments and sample sizes are described in STAR Methods and indicated in figures and/or figure legends. Data are plotted using the *ggplot2* package in R.